TECHNISCHE
UNIVERSITÄT
DRESDEN

Chaotic transport by a turnstile mechanism in 4D symplectic maps

Dissertation
zur Erlangung des wissenschaftlichen Grades
Doctor rerum naturalium

vorgelegt von

Franziska Hübner, geb. Onken
geboren am 21.03.1990 in Spremberg

Institut für Theoretische Physik
Fakultät Physik
Bereich Mathematik und Naturwissenschaften
Technische Universität Dresden
2020

Eingereicht am 23. Juni 2020

1. Gutachter: Prof. Dr. R. Ketzmerick
2. Gutachter: Prof. Dr. K. Padberg-Gehle

Abstract

Many systems in nature, e.g. atoms, molecules and planetary motion, can be described as Hamiltonian systems. In such systems, the transport between different regions of phase space determines some of their most important properties like the stability of the solar system and the rate of chemical reactions. While the transport in lower-dimensional systems with two degrees of freedom is well understood, much less is known for the higher-dimensional case. A central new feature in higher-dimensional systems are transport phenomena due to resonance channels. In this thesis, we clarify the complex geometry of resonance channels in phase space and identify a turnstile mechanism that dominates the transport out of such channels.

To this end, we consider the coupled standard map for numerical investigations as it is a generic example for 4D symplectic maps. At first, we visualize resonance channels in phase space revealing their highly non-trivial geometry. Secondly, we study the transport away from such channels. This is governed by families of hyperbolic 1D-tori and their stable and unstable manifolds. We provide an approach to measure the volume of a turnstile in higher dimensions as well as the corresponding transport. From the very good agreement of the two measurements we conclude that these structures are a suitable generalization of the well-known 2D turnstile mechanism to higher dimensions.

Zusammenfassung

Viele Systeme in der Natur, z.B. Atome, Moleküle und Planetenbewegungen, können als Hamilton'sche Systeme beschrieben werden. In solchen Systemen bestimmt der Transport zwischen verschiedenen Regionen des Phasenraums einige ihrer wichtigsten Eigenschaften wie die Stabilität des Sonnensystems und die Geschwindigkeit chemischer Reaktionen. Während der Transport in niedrigdimensionalen Systemen mit zwei Freiheitsgraden gut verstanden ist, ist für den höherdimensionalen Fall deutlich weniger bekannt. Eine zentrales neues Merkmal von höherdimensionalen Systemen sind Transportphänomene aufgrund von Resonanzkanälen. In dieser Arbeit verdeutlichen wir die komplexe Geometrie von Resonanzkanälen im Phasenraum und identifizieren einen Drehkreuzmechanismus, der den Transport aus einem solchen Kanal heraus dominiert.

Zu diesem Zweck betrachten wir die gekoppelte Standardabbildung für numerische Untersuchungen, da sie ein generisches Beispiel für 4D symplektische Abbildungen ist. Zuerst visualisieren wir Resonanzkanäle im Phasenraum und zeigen ihre höchst nicht-triviale Geometrie. Zweitens untersuchen wir den Transport weg von solchen Kanälen. Dieser wird durch Familien von hyperbolischen 1D-Tori sowie deren stabile und instabile Mannigfaltigkeiten bestimmt. Wir stellen einen Ansatz zur Messung sowohl des eingeschlossenen Volumens in höheren Dimensionen als auch des entsprechenden Transports vor. Aus der sehr guten Übereinstimmung der beiden Messungen schließen wir, dass diese Strukturen eine geeignete Verallgemeinerung des bekannten 2D Drehkreuzmechanismus in höheren Dimensionen sind.

Contents

1 Introduction 1

2 2D and 4D symplectic maps 5
- 2.1 Transport in 2D maps 5
- 2.2 4D example system: coupled standard map 9
- 2.3 Representations of 4D orbits 10
- 2.4 NHIMs 13

3 Resonance channels in 4D maps 15
- 3.1 Bifurcations of families of 1-tori 16
- 3.2 Skeleton of resonance channels 18
- 3.3 Transport away from resonance channels 20

4 Turnstile mechanism in 4D maps 21
- 4.1 Computation of a 4D turnstile 21
- 4.2 Volume measurement 28
- 4.3 Transport measurement 32
- 4.4 Comparison of volumes and transport 34

5 Numerical methods 39
- 5.1 Computation of 1-tori 39
- 5.2 Computation and manipulation of manifolds 42
- 5.3 Volumes and points in 3D 47

6 Summary and outlook 51

Appendix 53

A Ball method 55

B Triangulation method 59

Bibliography 63

1 Introduction

The field of dynamical systems reaches back to the 19th century [1]. Today it has a variety of applications ranging from atoms and molecules [2–4], chemical reactions [5–11], and particle accelerators [12–16] to the solar system [17,18], galaxies [18–21], and celestial mechanics [22–25] as well as the plasma confinement for fusion energy [26, 27]. In many situations these time-continuous systems can be reduced to time-discrete maps, either by means of a Poincaré surface of section or due to time-periodic external driving forces [28]. For example, an autonomous Hamiltonian system with f degrees of freedom leads to a $2f$-dimensional continuous system that can be reduced using energy conservation and a Poincaré section to a $(2f-2)$-dimensional map. The dynamics is then studied in the corresponding phase space, which is spanned by $f-1$ position coordinates and $f-1$ momentum coordinates [28].

In both, discrete and continuous systems, it is interesting to study transport phenomena, e.g. from one phase-space region to another or the escape from a region [29]. For example, in plasma physics this may correspond to the escape from the interior of a confinement device to the divertor [27]. Such long-range transport across the phase space is possible due to chaotic orbits, which exhibit exponential sensitivity to initial conditions. Consequently, chaotic transport is studied in terms of statistical features of ensembles of chaotic orbits with different approaches [29–31] instead of individual trajectories.

In generic situations the phase space has chaotic regions as well as regular regions and, thus, is called a mixed phase space. This coexistence strongly affects the transport in the system, e.g. chaotic orbits stick to the vicinity of regular structures, which is an effect termed trapping [32, 33]. In 2D maps, i.e. systems with $f = 2$ degrees of freedom, this is well understood in terms of partial barriers and the turnstile mechanism [29]. A partial barrier encloses a phase space region and is almost invariant under time evolution. Only a small fraction of phase space volume gets transported across a partial barrier in each iteration step at so-called turnstiles. More precisely, phase-space volume crosses the partial barrier from one side to the other through one lobe of the turnstile while, due to the volume conservation of symplectic maps, the same amount of volume crosses the barrier in opposite direction through the other lobe.

As most systems in nature have more than two degrees of freedom, the transport in higher-dimensional systems is an important topic. However, for transport mechanisms, it is crucial to understand the organisation of the phase space, which is more complicated for higher-dimensional maps [34]: In a $2k$-dimensional map, there are elliptic n-dimensional tori [35, 36], which are surrounded by (Cantor) families of elliptic $(n+1)$-dimensional tori [37, 38] with $n = 0, 1, \ldots, k-1$. For example, in 2D maps regular tori are 1D lines, which act as transport barriers. In contrast, in a 4D phase space elliptic 1D-tori, or 1-tori for short, are surrounded by regular 2-tori. This implies completely new features as the dimension of invariant regular 2-tori is insufficient to form a barrier for the chaotic transport in the 4D phase space. Consequently, chaotic orbits are able to get arbitrarily close to each point in phase space, i.e. by travelling through a net of resonance channels, the so-called Arnold web.

Resonance channels are a purely higher-dimensional phenomenon: While the transport along such a channel is described by Arnold diffusion [20, 39–42], much less is known about the transport out of resonance channels. In order to investigate this transport, it is necessary to study a resonance channel in phase space. This reveals complex structures, which are organised around families of 1-tori. These families can originate from the break-up of resonant 2-tori [43] or from bifurcations of other 1-tori due to resonances [44–46]. Moreover, bifurcations give rise to families of hyperbolic 1-tori, also called whiskered tori [39, 47] as they have attached 2D stable and unstable manifolds. The general concept describing the invariant manifold, on which a family of hyperbolic 1-tori is located, is called normally hyperbolic invariant manifold (NHIM) [8, 48].

The aim of this thesis is to understand the transport out of a resonance channel by a turnstile mechanism in higher dimensions. Our approach is based on a partial barrier composed of 2D invariant manifolds attached to hyperbolic 1-tori. These 2D objects alone cannot be a barrier in a 4D space as for this a codimension one is essential. Thus, we consider the whole one-parameter family of 1-tori whose manifolds form a 3D barrier. Due to intersections of the manifolds arises a transport across the partial barrier, which is the analogue to the turnstile mechanism in 2D maps. We quantify this transport and find a good agreement of the measured transport and the volume of a turnstile lobe apart from crossing resonances. Hence, the given construction is a suitable generalisation of the turnstile mechanism in a 4D map.

In Chap. 2 we first introduce 2D maps and the turnstile mechanism in 2D. Secondly, we define the coupled standard map as an example for a generic 4D map with mixed phase space. Then, different solutions for the problem of visualising a 4D system are given. In addition, we introduce more details on NHIMs. Chapter 3 deals with the organisation of the 4D phase space in more detail in terms of resonance channels. In the first part we study bifurcations of families of 1-tori, which leads to the skeleton of a resonance channel. Furthermore, we show a first investigation of the influence of the 1-tori and their manifolds on the transport away from a resonance channel.

In Chap. 4 we describe the turnstile mechanism in higher dimensions starting with details of the barrier construction. On one hand, the enclosed volume of a turnstile lobe is a prediction for the transport through the partial barrier. On the other hand, the transport can be measured with a large ensemble of initial conditions. The comparison of volumes and transport measurements reveals a good agreement where it was expected. The deviations at crossing resonances are due to the resonance gaps of the barrier, which are filled by a linear interpolation in this thesis. In addition, the results are compared with a different method based on NHIMs, which also fit very well.

In Chap. 4 the numerical details are omitted and collected separately in Chap. 5. The first part deals with the computation of 1-tori while the second section explains the growing, interpolation, intersection, and cropping of manifolds. Thirdly, the measurement of volumes and the handling of point ensembles is described.

A summary is given in Chap. 6, where we also discuss possible subsequent investigations. Finally, the two appendices introduce alternative methods to measure volumes and start point ensembles in a 4D space.

2 2D and 4D symplectic maps

This chapter introduces the classical mappings that are the chosen dynamical system of this thesis. We are interested in a regime of a mixed phase space, where regular and chaotic dynamics coexists. In general, the structures of such a mixed phase space are governed by the Kolgomorov–Arnold–Moser theorem and the Poincaré–Birkhoff theorem [49].

The transport properties of chaotic motion in a system with mixed phase space are very different from the transport properties in a fully chaotic system. While chaotic orbits in the globally chaotic system explore the phase space rather uniformly, they remain longer in the vicinity of the regular regions in mixed systems. For 2D maps this is explained by the concept of partial transport barriers [50], which is introduced in Sec. 2.1.

To study transport in four dimensions, a suitable model system is needed. We employ two coupled standard maps as this is considered as a generic example for 4D symplectic maps. The definition of the 4D standard map and some phase-space structures are given in Sec. 2.2.

A fundamental problem of 4D systems is their visualisation. Section 2.3 introduces three different approaches to overcome this difficulty, namely 3D phase-space slices, the method of colour and rotation and the frequency space.

The generic concept of normally hyperbolic invariant manifolds, so-called NHIMs, plays an important role for the chaotic transport in higher dimensional systems. Some details, definitions and hints for a numerical computation are given in Sec. 2.4.

2.1 Transport in 2D maps

The transport in deterministic dynamical systems is usually studied by long-time statistics like exit-time distributions [29]. That is, many points are started in phase space and iterated until they reach an exit region. The distribution of exit times then depends on the structures present in the system. In mixed systems, where chaotic and regular dynamics coexists, the exit times follow a power-law distribution. This can be understood by a superposition of exponential decays due to partial barriers [50]. These partial barriers cause chaotic orbits to stay longer in the enclosed region as in each iteration step only a small phase space volume is transported across the barrier.

Such a partial barrier can originate from different phase space structures [50]: periodic orbits, homoclinic points, and cantori. Important is their dimensionality as only objects of codimension one can be a barrier. Hence, in a 2D space a barrier is a 1D line. In this sense, a partial barrier arises for instance from a line connecting periodic orbits or homoclinic points. In the following, we focus on barriers build by the 1D invariant manifolds of a hyperbolic fixed point, which intersect in homoclinic points.

As an example serves the 2D Chirikov standard map f_{2D} [51]

$$\begin{aligned} p' &= p + \frac{K}{2\pi}\sin(2\pi q') + 0.5 \quad \mod 1 \quad - 0.5 \\ q' &= q + p \quad \mod 1 \end{aligned} \tag{2.1}$$

with periodic boundary conditions, such that $p \in [-0.5, 0.5)$ and $q \in [0, 1)$, at kicking strength $K = 1.8$. In Fig. 2.1 the hyperbolic fixed point at $u = (p_u, q_u) = (0, 0)$ is shown in green and its 1D stable and unstable manifolds in red and blue, respectively. Note that the fixed point is also visible at $(p, q) = (0, 1)$ due to the periodic boundary conditions.

The stable manifold W^s is defined as the set of points that converges exponentially towards the fixed point under forward iteration. Similarly, the unstable manifold W^u converges to the fixed point under backward iteration. Locally, i.e. close to the fixed point, the manifolds can be computed from the eigenvectors ψ of the linearised map at the fixed point. In doing so, the Hartmann-Grobmann theorem guarantees that the linearisation is tangent to the actual manifolds. Numerically the manifolds can be determined by iterating n_p points started on the vector $u + h\psi$, where h is a small factor. As the distance between the points on the manifold grows exponentially with the iterations, the parameters h and n_p determine the precision of the computed manifold. The number of iterations n_s affects their length.

If the manifolds are computed long enough, they intersect in a homoclinic point. The parts of the manifolds from the fixed point to their first intersections (yellow points) define the resonance zone (grey area) with area A_{rz}. Further iteration of the manifolds leads to more intersections (orange points). Between the repeated intersections arise turnstiles consisting of two lobes. One lobe is for instance the green area between the first (yellow) and the second (orange) intersection. The value of K is chosen such that these lobes are as big as possible, but at the same time not affected by the periodic boundary conditions. Note that "first" and "second" intersection are not well-defined but rather a choice made here.

The border of the grey region is a *partial barrier* as most initial conditions will stay inside when iterated. Only the hatched upper exit set E_u and its lower counterpart E_l will leave the resonance zone in one iteration. The green area is the image of the set E_u and, as the standard map is symplectic, the green region and E_u have the same area A_t. Hence, this area is transported across the partial barrier in one iteration step, which is referred to as *flux*. Due to area conservation the same amount of phase space volume has to enter the resonance zone in one step. The incoming sets are labelled as I^u and I_l in Fig. 2.1. This interplay of entering and leaving phase space volume is the origin of the denomination "turnstile". Note that in case of periodic points of period p indeed p turnstiles arise, but in one map iteration only one of them is relevant [29].

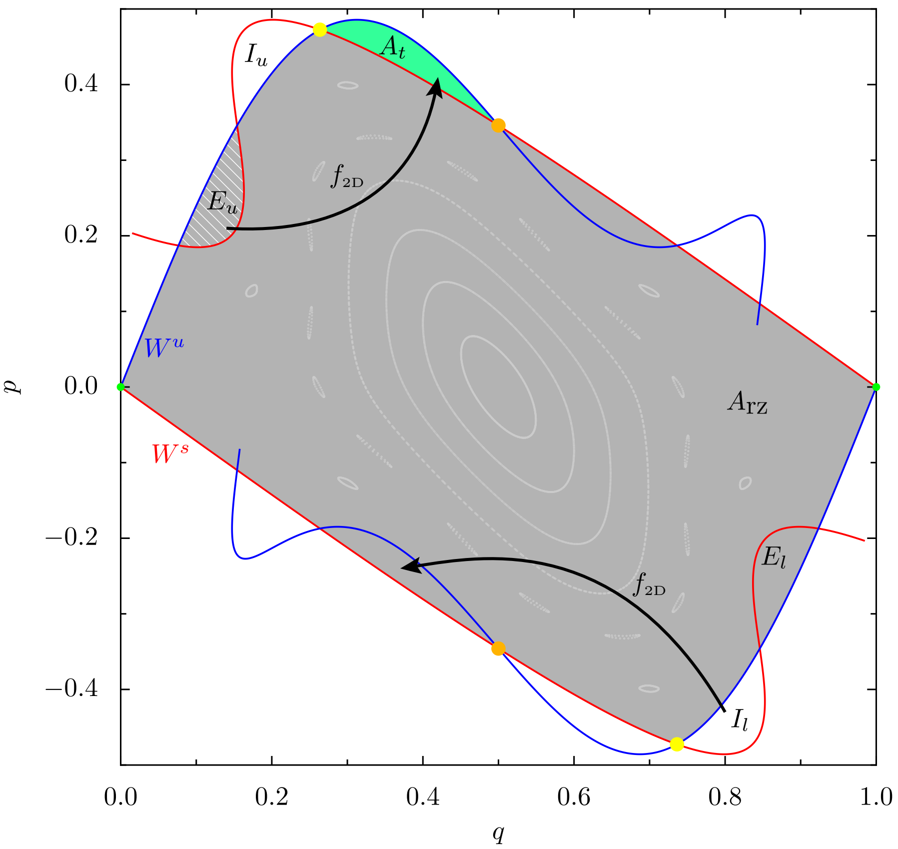

Figure 2.1: Phase space of the 2D standard map f_{2D} for $K = 1.8$. The hyperbolic fixed point is shown in green and its stable W^s and unstable W^u manifolds in red and blue, respectively. Their intersections are marked by yellow (first) and orange (second) points. The grey area A_{rz} is the enclosed resonance zone including the hatched exit set E_u. The image of E_u is the green area A_t. The light-coloured lines are the regular structures.

There are multiple ways to compute the flux in 2D maps: approximate the turnstile area by a polygon, measure the turnstile area with uniformly distributed points, and using the action of orbits [29, Sec. 4], [50, 52–54]. More details for each approach are explained in the following.

Action

The action of an orbit segment from q to q' can be calculated with the generating function $F(q, q')$ of the map. For the standard map f_{2D} it reads

$$F(q, q') = \frac{1}{2}(q - q')^2 - \frac{K}{4\pi^2}\cos(2\pi q')$$

The action of the whole orbit is the sum over all segments or rather all iteration steps $s \in (-\infty, \infty)$. In general, the action describes the area under a curve. The turnstile area is equal to the action difference $A_t = \sum_s \Delta F_s$ as it results from the difference of the area under the partial barrier and under the iteration of the barrier. In detail, the action difference reads

$$\Delta F_s = F(w_s, w_{s+1}) - F(z_s, z_{s+1}).$$

The orbits to use as w_s and z_s are the homoclinic intersection. We choose w_0 to be the first intersection (yellow) and z_0 the second intersection (orange). Finally, numerically only a finite number of iterations is considered and the turnstile area is determined by

$$A_t = \sum_{s=-n_i}^{n_i} \Delta F_s.$$

This method is considered very accurate [50] and less prone to numerical errors than the other two methods. For the standard map f_{2D} at $K = 1.8$ the action method yields a turnstile area of $A_t = 0.00704604$.

In case the manifolds and their intersections are not known, also periodic orbits of high period p can be used as they approximate the partial barrier. Then, the area A_t is the action difference of the minimizing and the minimax orbit $A_t = \sum_{t=0}^{p-1} \Delta F_t$ with w_t the minimax orbit and z_t the minimizing orbit.

This method was adapted to 3D maps [55] and recently also to 4D maps [56]. In the 4D case the periodic orbits are replaced by periodic NHIMs, which are explained in Sec. 2.4.

Area

The area method means to numerically determine points on the border and then compute the area of the enclosed polygon. The area of a n-polygon spanned by $(x_i, y_i), i = 0, \ldots, n-1$ is given by the shoelace formula also known as Gauss's area formula [57]

$$A = \frac{1}{2} \left| \sum_{i=0}^{n-1} (y_i + y_{i+1 \bmod n})(x_i - x_{i+1 \bmod n}) \right| .$$

Here, x and y are replaced by p and q. For convex shapes this method tends to slightly underestimate the area. In case of the example map the polygon area $A_t = 0.00704259$ is very close to the value from the action method.

Points

The point method relies on the fact that an area $\tilde{A}$ can be measured by a number of points N with constant density ρ, i.e. $\tilde{A} = N\rho$. The density of points is set by the total number of points N_{g} in the phase space volume $\rho = V_{\mathrm{ps}}/N_{\mathrm{g}}$. For the example map f_{2D} the phase space volume is $V_{\mathrm{ps}} = 1$. Hence, N_t points in the turnstile correspond to $\tilde{A}_t = N_t/N_{\mathrm{g}}$.

As a special case of uniformly distributed points we use a grid. In order to get $N_{\mathrm{w}} = 10^5$ points, a grid with $\lfloor\sqrt{N_{\mathrm{w}}}\rceil = 316$ points per direction is needed. From the resulting $N_{\mathrm{g}} = 99856$ grid points we find $N_t = 710$ in the upper turnstile, which leads to $\tilde{A}_t = 0.00711024$. Compared to the result of the action method this corresponds to an absolute error of $6.4 \cdot 10^{-5}$, which is below the expected deviation of $\sqrt{N_t}/N_{\mathrm{g}} = 2.7 \cdot 10^{-4}$.

Another way of studying the transport is to measure the transport rate. Based on the areas the expected rate is $r = A_t/A_{\mathrm{rz}} = 0.0135364$ for each turnstile. Hence, if we start N_0 points inside the resonance zone (grey region) and iterate them once, then we expect $N_t = N_0 r$ points to leave the region over the upper turnstile. Using the same grid as above for the example map, we get $N_0 = 51983$ points in the resonance zone. With the rate from the areas 704 points are expected to leave through each turnstile. After one iteration with the map $f_{2\mathrm{D}}$, 1416 points left the resonance zone. One half of them left through the upper turnstile and the other half through the lower one. Thus, in this experiment $N_t = 708$, $\tilde{A}_t = 0.00709021$ and $r = 0.01361984$. The error of the turnstile lobe area $\tilde{A}_t$ is relative to the results of the action method 0.63% and relative to the area method 0.67%.

The comparison of areas and points is a good way to verify the turnstile mechanism as the two results match only, if there is no additional transport across the boundary of the resonance zone. In this sense, this thesis studies the turnstile mechanism in a 4D map by adjusting the two methods to higher dimensions.

2.2 4D example system: coupled standard map

A 4D phase space is spanned by two momenta p_1, p_2 and two positions q_1, q_2, i.e. one pair of coordinates (p, q) for each degree of freedom. For the studies of this thesis we used two coupled standard maps [58], $\mathcal{F}\colon (p_1, p_2, q_1, q_2) \mapsto (p_1', p_2', q_1', q_2')$,

$$\begin{aligned}
p_1' &= p_1 + \frac{K_1}{2\pi}\sin(2\pi q_1') + \frac{\xi}{2\pi}\sin(2\pi(q_1' + q_2'))\\
p_2' &= p_2 + \frac{K_2}{2\pi}\sin(2\pi q_2') + \frac{\xi}{2\pi}\sin(2\pi(q_1' + q_2'))\\
q_1' &= q_1 + p_1\\
q_2' &= q_2 + p_2,
\end{aligned} \tag{2.2}$$

where $p_{1,2} \in [-0.5, 0.5)$, $q_{1,2} \in [0, 1)$ and periodic boundary conditions are imposed in each coordinate analogue to Eq. (2.1). The resulting map is symplectic. The parameters K_1 and K_2 control the non-linearity of the individual 2D standard maps in (p_1, q_1) and (p_2, q_2), respectively. The parameter ξ introduces a coupling between the two degrees of freedom. The studies in Chap. 4 are executed with $K_1 = 1.8$, $K_2 = 0$ and the coupling ξ varied between 0.01 and 0.15. These values yield a map that is suited to study the transport. For the visualisations in

Sec. 2.3 and Chap. 3 the parameters $K_1 = 2.25$, $K_2 = 3$ and $\xi = 1$ are used. These stronger perturbations lead to a generic example of a mixed system with a regular island embedded in the chaotic sea.

In 2D maps the regular orbits are 1D lines, see for instance the light grey lines in Fig. 2.1, which are organised around elliptic fixed points (not shown). The organisation of a 4D phase space is more complicated [34]: regular orbits are 2-tori that are arranged around elliptic 1-tori. These occur as one-parameter families either from bifurcations, see Sec. 3.2, or attached to elliptic-elliptic fixed points. In addition, fixed points can be unstable, i.e. hyperbolic-hyperbolic, or have one of the mixed stabilities hyperbolic-elliptic or elliptic-hyperbolic. Furthermore, there are one-parameter families of hyperbolic 1-tori. Similar to their elliptic counterparts, they arise from bifurcations or from fixed points with mixed stability. Hyperbolic 1-tori play an important role in this thesis as they somehow organise the chaotic motion. This is explained in detail in Chap. 3.

2.3 Representations of 4D orbits

A fundamental problem of 4D systems is their visualisation. This section introduces different approaches to overcome this difficulty. The first one is to reduce the depiction of phase space to three dimensions. To this end, two methods are explained in Sec. 2.3.1 starting with 3D phase-space slices, which are well suited to visualise many orbits at once. The disadvantage of this method is the loss of information due to the reduction of dimensions. A full-dimensional representation is achieved by the second method called "method of colour and rotation". A detailed comparison of both methods can be found in Ref. [59, Sec. II.B.1].

A completely different approach is the frequency space explained in Sec. 2.3.2. By describing regular tori with frequencies the system is reduced to a 2D plane. In addition, this representation makes resonances clearly visible.

2.3.1 Phase space

3D phase-space slices were introduced by Richter et al. [59]. The idea is to plot only those points of an orbit that fall in a thickened hyperplane Γ. This leads to a reduction of the dimension by one as sketched in Fig. 2.2. Typically, a 2-torus (grey) is reduced to rings (black) and a 1-torus (blue) to points (orange).

For the 4D standard map $\mathcal{F}$ with $K_1 = 2.25$, $K_2 = 3$ and $\xi = 1$ the plane defined by

$$\Gamma_\varepsilon = \Big\{ (p_1, p_2, q_1, q_2) \;\Big|\; |p_2 - p_2^*| \leq \varepsilon \Big\} \tag{2.3}$$

with $p_2^* = 0$ and $\varepsilon = 10^{-4}$ is suitable as it captures most of the structures. As an example, some regular orbits on 2-tori are shown in Fig. 2.3 as grey rings and elliptic 1-tori as orange

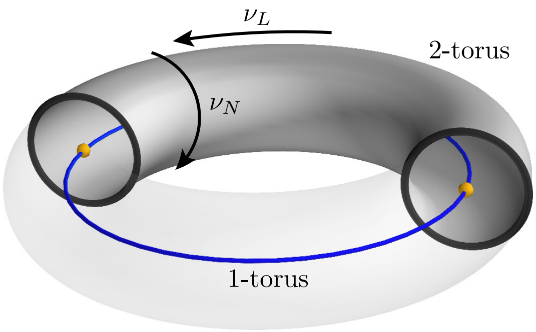

Figure 2.2: Sketch of a 2-torus (grey), a 1-torus (blue) and their representations in a 3D phase-space slice (black, orange).

points. Note that the 1-tori occur as one-parameter families and hence, appear as lines. The two families $\mathcal{M}_1^{\text{fp}}$ and $\mathcal{M}_2^{\text{fp}}$ labelled in Fig. 2.3 are attached to the elliptic-elliptic fixed point at $(p_1, p_2, q_1, q_2) = (0, 0, 0.5, 0.5)$.

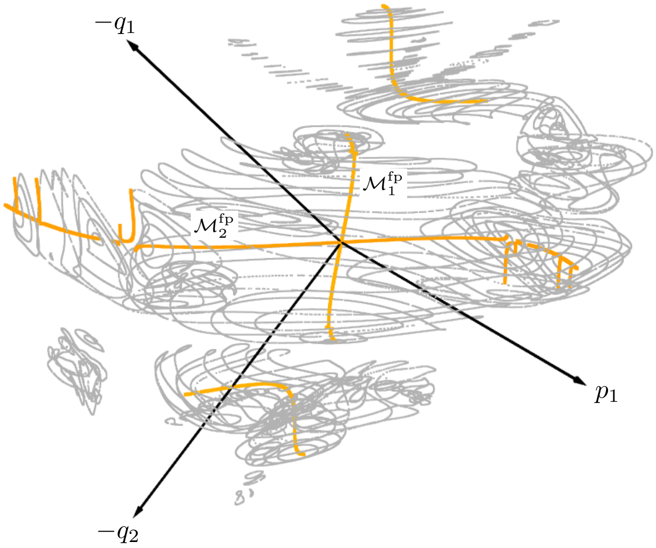

Figure 2.3: 3D phase-space slice of regular structures of map $\mathcal{F}$ with $K_1 = 2.25$, $K_2 = 3$ and $\xi = 1$. The grey rings are 2-tori and the orange lines are composed of many points representing 1-tori. The origin is at $(p_1, q_1, q_2) = (0, 0.5, 0.5)$. This figure is similar to Refs. [46, Fig. 1] and [34, Fig. 3].

The method of colour and rotation [60, 61] is a projection to a 3D space with the missing coordinate encoded as colour. This is useful to visualise the geometry of single objects in the full space, but not suited to depict many orbits at once. Several examples for the map $\mathcal{F}$ can be found in Ref. [59].

2.3.2 Frequency space

The regular motion on a 2-torus can be described by a longitudinal frequency ν_L and a normal frequency ν_N as indicated in Fig. 2.2. The result of a numerical frequency analysis [17, 62] for the strongly perturbed map $\mathcal{F}$ is shown in Fig. 2.4 as grey points, see Ref. [46] for details. Note that the correspondence of ν_1 and ν_2 to ν_L and ν_N depends on the region. For orbits in the vicinity of the lower orange line $\nu_1 \equiv \nu_L$ and $\nu_2 \equiv \nu_N$. Close to the upper orange line it is the other way around.

The motion on a 1-torus is characterised by one longitudinal frequency. For elliptic 1-tori a normal frequency can be defined either via surrounding 2-tori [63] or by means of the linearised dynamics [64, 65]. This way, they can be included in the frequency space as orange lines.

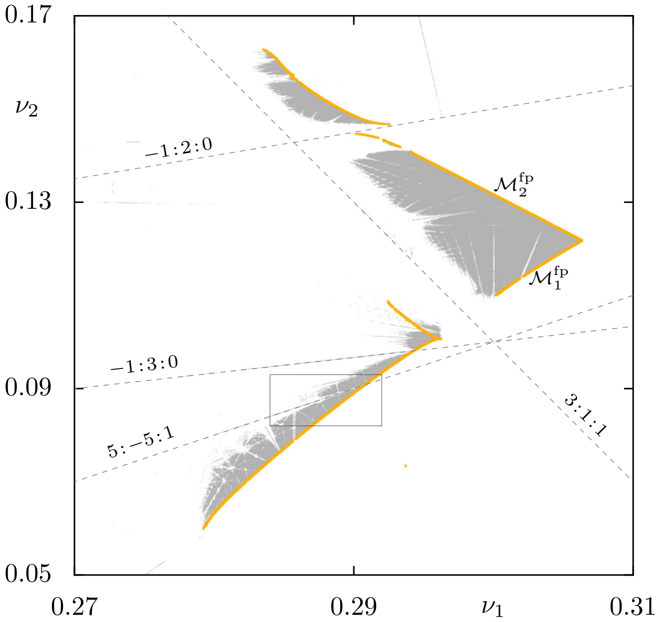

Figure 2.4: Frequency space of map $\mathcal{F}$ based on 10^8 initial conditions with randomly chosen $p_1, p_2 \in [-0.2, 0.2]$, $q_1, q_2 \in [0.3, 0.7]$. Regular orbits are represented by grey points and the two families of elliptic 1-tori are shown as orange lines. The dashed lines are resonances labelled with $m_1 : m_2 : n$. The black box indicates a magnification shown in Fig. 3.2(a).
This figure is similar to Refs. [46, Fig. 3], [34, Fig. 3], [59, Fig. 4].

A line in frequency space described by $m_1 \cdot \nu_1 + m_2 \cdot \nu_2 = n$, where m_1, m_2, n are integers without common divisor, is called a resonance line. While there are infinitely many of them covering the frequency space, only a few important examples are included as dashed lines and labelled with $m_1 : m_2 : n$ in Fig. 2.4. These resonances lead to so-called *resonance channels* and bifurcations, which are described in Chap. 3 in more detail. In general, the resonances and their corresponding bifurcations lead to gaps in the families of 1-tori making them actually Cantor families.

2.4 NHIMs

Normally hyperbolic invariant manifolds (NHIMs) play an important role for the chaotic transport in higher dimensional systems as they are a higher dimensional analogue of hyperbolic fixed points [66–71]. For instance, a one-parameter family of hyperbolic 1-tori in a 4D map lies on a 2D NHIM. Note that the family is actually a Cantor family due to crossing resonances and that the continuous NHIM is present inside these gaps as well.

A n-dimensional NHIM has attached $(n+1)$-dimensional stable and unstable invariant manifolds that influence the dynamics in the normal directions of the NHIM. For instance, a hyperbolic 1-torus has attached 2D invariant manifolds and a 2D NHIM, as the example given above, has 3D stable and unstable manifolds. Initial conditions on the invariant manifolds converge exponentially towards the NHIM under forward or backward iteration. More precisely, these manifolds are fibrations of families of stable and unstable fibres to each point on the NHIM. The manifolds are invariant in the sense that each fibre is mapped into another single fibre.

The dynamics on the NHIM itself can be very complex including fixed points or chaotic motion, which may expand or contract. If the contraction/expansion rate is stronger than the rate normal to the NHIM, the NHIM will get holes.

The numerical construction of a NHIM with a binary contraction method is described in Ref. [72]. To this end, the position of the four invariant manifolds needs to be known roughly. Then, in each of the quadrants generated locally by the manifolds one point is started. They are the initial points for a bisection method converging to a point on the NHIM.

3 Resonance channels in 4D maps

Resonance channels are crucial structures for the transport in higher-dimensional systems [48]. The first studies about transport along a resonance channel reach back to work by Vladimir Arnol'd from 1964 [39]. He described the diffusion process due to heteroclinic intersections of the invariant manifolds of hyperbolic 1-tori, later termed *Arnold diffusion.* The same mechanism allows a chaotic orbit to move from one channel to another at junctions. In this way all channels are connected and form the so-called *Arnold web.* As resonance channels occur on arbitrary fine scales, a chaotic orbit can get arbitrary close to each point in a higher-dimensional phase space [28, 73].

As Arnold diffusion along resonance channels is expected to be very slow, this thesis focuses on the transport in the perpendicular direction, i.e. "away from" or "out of" the resonance channel. The transport in this direction is restricted by partial barriers composed of the stable and unstable manifolds of hyperbolic 1-tori, which we show in detail in Chap. 4. This is in some sense similar to a resonance in a 2D map, which leads to stable and unstable periodic points according to the Poincaré–Birkhoff theorem [28, 74]. The invariant manifolds of the unstable points form a partial barrier as explained in Sec. 2.1. Even though there is no direct generalisation of the Poincaré–Birkhoff theorem to more degrees of freedom, the fate of a resonant torus is known [34, 43]. If a 2-torus fulfils one resonance condition, it breaks up in elliptic and hyperbolic 1-tori. As in general a family of 2-tori fulfils a resonance condition, this is one origin of families of hyperbolic 1-tori.

A different approach to study resonances are bifurcations. To this end an external parameter has to be varied in 2D maps. In contrast, in a 4D map all stages of a bifurcation are included at fixed parameters. Here, the longitudinal frequency, which varies along the family of 1-tori, plays the role of the bifurcation parameter. The bifurcations occurring when such a family crosses a resonance [44, 45] are associated with resonance channels as we published in Ref. [46], see also Ref. [75]. The system studied there is the strongly coupled standard map, see Sec. 2.3. A short summary of Ref. [46] is given in Sec. 3.1, while in Sec. 3.2 the generic case of bifurcations is reviewed more closely. The knowledge about phase-space structures in resonance channels allows to study the transport away from the channel in terms of escape time plots, presented in Sec. 3.3.

3.1 Bifurcations of families of 1-tori

If a family of 1-tori crosses a resonance, i.e. the frequencies of a 1-torus in the family fulfil a resonance condition, bifurcations occur. They give rise to gaps, bends, and emerging branches. In this process, the bifurcation parameter is the longitudinal frequency ν_L of the 1-tori that varies along the family.

In Ref. [46] a system of two strongly coupled standard maps is considered, see also Sec. 2.3. Recall, that this system has two elliptic main families $\mathcal{M}_1^{\text{fp}}$ and $\mathcal{M}_2^{\text{fp}}$, visible as orange lines in a phase-space slice (Fig. 2.3) and in frequency space (Fig. 2.4). In terms of the frequencies of 1-tori a resonance is described by $m_L \cdot \nu_L + m_N \cdot \nu_N = n$ with the normal frequency ν_N and m_L, m_N and n integers without common divisor. The absolute value of the coefficient m_N is the crucial parameter to categorise bifurcations. In agreement with normal form studies [45] we distinguish the following cases: $|m_N| = 0$ (gaps), $|m_N| = 1$ (bends), $|m_N| = 2$ (gaps), $|m_N| = 3$ (branches), $|m_N| \geq 4$ (branches). Figure 3.1 shows examples for all cases in a 3D phase-space slice. The following provides short descriptions, which are close to Ref. [46].

$\boldsymbol{|m_N| = 0}$ This case relates to a rational value of the longitudinal frequency. Very similar to the Poincaré–Birkhoff scenario [28] in 2D maps, an elliptic 1-torus breaks up in a chain of periodic points with alternating elliptic-elliptic and elliptic-hyperbolic stability. As an example Fig. 3.1(a) shows the 7 : 0 : 2 resonance crossing the main family $\mathcal{M}_1^{\text{fp}}$. Analogue to the 2D case not only the rational 1-torus itself breaks, but also the 1-tori in its vicinity. The resulting gap is filled by new structures around the periodic points. Note that the $|m_N| = 0$ case is the only one that also affects hyperbolic 1-tori, which have solely a longitudinal frequency. They break up in hyperbolic-hyperbolic and elliptic-hyperbolic periodic points. The latter have attached families of hyperbolic 1-tori, which establishes a hyperbolic hierarchy.

$\boldsymbol{|m_N| = 1}$ This kind of bifurcations causes prominent bends in a family of elliptic 1-tori on either side of the crossing resonance, which leads to pronounced gaps. While the elliptic branch on one side of the gap just bends, the one on the other side gets hyperbolic at some point. One example is the 3 : 1 : 1 resonance crossing $\mathcal{M}_1^{\text{fp}}$ shown in Fig. 3.1(b).

$\boldsymbol{|m_N| = 2}$ Bifurcations with $|m_N| = 2$ cause a different kind of gap in the main family of elliptic 1-tori, namely that the family contains a segment of hyperbolic 1-tori: Firstly, the main family of elliptic 1-tori changes its stability to hyperbolic while an elliptic family emerges, appearing as two branches in the 3D phase-space slice. Secondly, the main family of now hyperbolic 1-tori becomes elliptic again and a hyperbolic family emerges, also appearing as two branches in the 3D phase-space slice. As an example the the -2 : 10 : 1 resonance crossing $\mathcal{M}_2^{\text{fp}}$ is shown in Fig. 3.1(c).

$|m_N| = 3$ In Fig. 3.1(d) the $-1 : 3 : 0$ resonance crossing $\mathcal{M}_1^{\mathrm{fp}}$ serves as an example. Bifurcations with $|m_N| = 3$ are more complicated: Initially, an elliptic and a hyperbolic family of 1-tori emerge in a saddle-node bifurcation. In Fig. 3.1(d) this is where the red and the green family meet. Note that each family appears in a 3D phase-space slice as three branches. From the meeting point the red elliptic family continues outwards while the green hyperbolic family collapses at the orange main family and re-emerges from it. Thus, the region close to the orange family is considerably deprived of regular tori.

$|m_N| \geq 4$ This is the generic case, in which $|m_N|$ elliptic and $|m_N|$ hyperbolic branches emerge. As an example in Fig. 3.1(e) serves the $5 : -5 : 1$ resonance crossing $\mathcal{M}_1^{\mathrm{fp}}$, which corresponds to $|m_N| = 5$. A more detailed explanation of this case is given in Sec. 3.2.

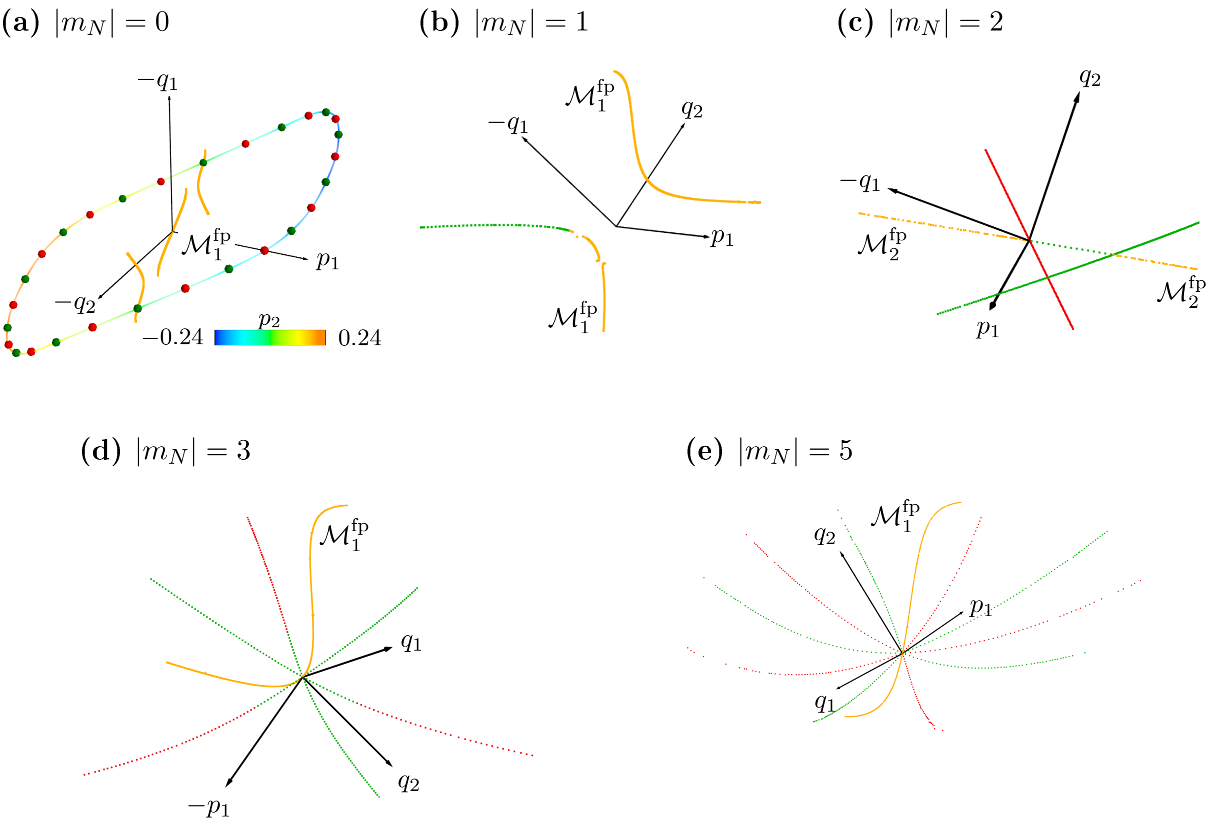

(a) $|m_N| = 0$ **(b)** $|m_N| = 1$ **(c)** $|m_N| = 2$

(d) $|m_N| = 3$ **(e)** $|m_N| = 5$

Figure 3.1: Bifurcations in a 3D phase-space slice. In all figures the orange lines are the main families of elliptic 1-tori as in Fig. 2.3. The emerging red families are elliptic and the green ones are hyperbolic. In (a) a chain of elliptic-elliptic (red) and elliptic-hyperbolic (green) periodic orbits is shown. In addition, a projection of a near by 1-torus is depicted with the p_2-coordinate encoded as colour.

In Ref. [46] we discuss two additional aspects, regarding symmetry breaking bifurcations and one resonance crossing both main families of elliptic 1-tori. The presence of symmetries in a map leads to additional kinds of bifurcations. In the example system we observe two $|m_N| = 1$ bifurcations with unexpected behaviour. The $-1 : 2 : 0$ resonance intersecting $\mathcal{M}_2^{\mathrm{fp}}$ shows an effect similar to a $|m_N| = 2$ resonance, but with dynamically separated emerging branches. These branches can be mapped on each other by one symmetry of the map. The $-1 : 10 : 1$ resonance intersecting $\mathcal{M}_2^{\text{fp}}$ looks like a $|m_N| = 4$ bifurcation, i.e. it is a double symmetry breaking bifurcation. The four emerging branches of each stability are again dynamically not connected, but linked pairwise by the two symmetries of the map.

While in general a resonance channel $m_1 : m_2 : n$ crosses only one of the main families of 1-tori, it is also possible that both families are involved. In this case, locally at each crossing point the bifurcations behave as described above, one with $m_N = m_1$ and one with $m_N = m_2$. The geometry along the connection is non-trivial as the structures have to alter continuously, such that the coefficients m_1 and m_2 switch their roles. From a geometrical point of view, a 2-torus with large radius r_1 and small radius r_2 has to fade into one with large radius r_2 and small radius r_1.

3.2 Skeleton of resonance channels

Resonance channels arise due to resonant frequencies as explained in Sec. 2.3.2 and in the previous section. The structures in a channel can be studied from two different points of view: firstly, as the break-up of resonant 2-tori [43] and secondly, as bifurcations of families of 1-tori. Of course, both approaches explain the phase-space structures consistently.

The break-up of resonant 2-tori results in families of elliptic and hyperbolic 1-tori along the channel [43], which is also predicted by bifurcations as explained above in Sec. 3.1. The families of 1-tori build the skeleton of the resonance channel in the following sense: Around the elliptic 1-tori again regular 2-tori arise, which implies a self-similar phase space structure. The hyperbolic 1-tori have 2D invariant manifolds attached that rule the chaotic transport away from the channel as discussed in detail in Chap. 4.

In order to illustrate the resonance channel in phase space, we consider the $5 : -5 : 1$ resonance in the map $\mathcal{F}$ with $K_1 = 2.25$, $K_2 = 3$ and $\xi = 1$ [46]. This system is introduced in Sec. 2.3. We illustrate a magnification of the frequency space around the $5 : -5 : 1$ resonance and the main family $\mathcal{M}_1^{\text{fp}}$ in Fig. 3.2(a), corresponding to the indicated box in Fig. 2.4. Each grey point represents a 2-torus, the resonance is marked by a dashed line and the main family of elliptic 1-tori $\mathcal{M}_1^{\text{fp}}$ is depicted in orange. The same structure is shown in a 3D phase-space slice in Fig. 3.2(b). Note that the 1-tori appear as points and a one-parameter family of them forms a line, see e.g. the orange family $\mathcal{M}_1^{\text{fp}}$. Exactly from the point where $\mathcal{M}_1^{\text{fp}}$ crosses the resonance line, there emerge new families of 1-tori, namely five elliptic (red) and five hyperbolic (green) ones. In frequency space the new families are on the resonance line. For the elliptic 1-tori two frequencies are assigned as explained in Sec. 2.3.2. As hyperbolic 1-tori have only one frequency, they cannot be included in the frequency space directly. However, they have an elliptic partner with the same longitudinal frequency.

The dynamics in the vicinity of this structure is studied with local 2D projections shown in Fig. 3.2(c) to (e). To this end, orbits in the 3D phase-space slice are projected to a 2D plane, which does not alter their dimensionality. Hence, a 2-torus is shown as grey ring as in Fig. 2.3. The emerging 1-tori are represented by red, orange and green points. They correspond to the highlighted bigger points already shown in (b) and to the encircled letters in (a). Furthermore, in Fig. 3.2(d) and (e) some iterations of a chaotic orbit are depicted in blue.

The red and orange elliptic 1-tori organise the regular motion as around every 1-torus exists a family of 2-tori (grey). This is visible in all 2D projections Fig. 3.2(c) to (e). In some sense, the hyperbolic 1-tori organise the chaotic dynamics. Although there is no surrounding 2-torus in Fig. 3.2(e), the chaotic orbit stays close to the resonance for some time. This indicates the presence of a partial barrier, which is composed of the invariant manifolds of the hyperbolic 1-tori. We present further numerical support for this hypothesis in the following section.

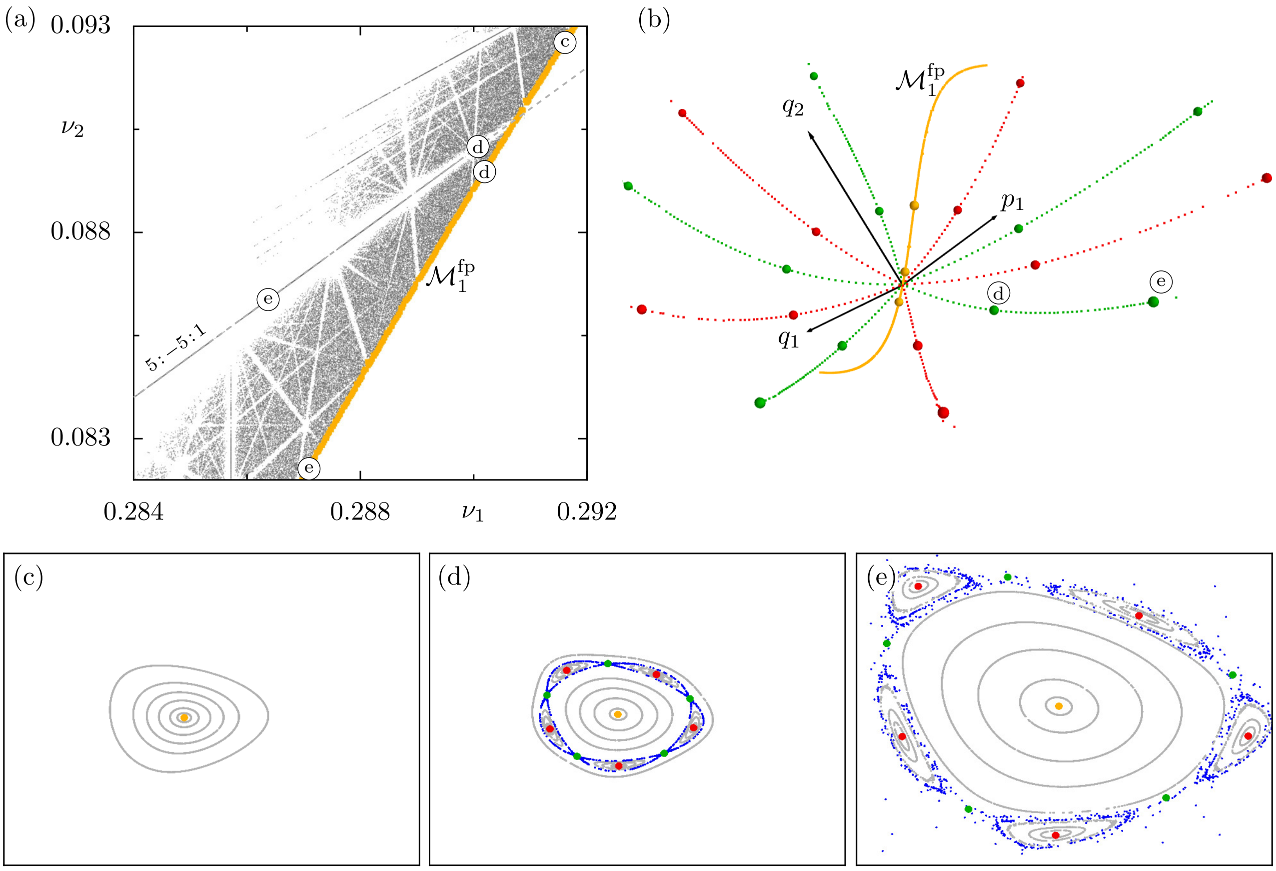

Figure 3.2: Visualization of the $5 : -5 : 1$ resonance intersecting $\mathcal{M}_1^{\mathrm{fp}}$. (a) Zoom of frequency space shown in Fig. 2.4. (b) Zoom of 3D phase-space slice in Fig. 2.3 with elliptic (red, orange) and hyperbolic 1-tori (green). (c)–(e) Sequence of local 2D projections from the 3D phase-space slice onto a plane with regular 2-tori (grey rings), elliptic 1-tori (red, orange), and hyperbolic 1-tori (green). The 1-tori appearing in the local 2D projections (coloured points) are marked by encircled letters in (a) and by larger spheres in (b). The planes (c)–(e) have normal vector $\vec{n} = (p_1, q_1, q_2) = (-0.338, -0.644, 0.687)$. The phase space coordinates (p_1, p_2, q_1, q_2) of the orange points are (c): $(0, 0, 0.457, 0.578)$, (d): $(0, 0, 0.453, 0.581)$, and (e): $(0, 0, 0.447, 0.587)$.

3.3 Transport away from resonance channels

In order to study the transport away from a resonance channel, we utilize escape times. That is, many points are started in the region of interest and iterated until they reach some exit region located deep in the chaotic sea. The time needed to escape t_{esc} is assigned to the initial point and encoded in colours.

For such an illustration we start initial conditions on the plane from Fig. 3.2(e). To include a larger vicinity of the structure, the plane is enlarged by a factor of 1.5. As exit region we use the cuboid $\{(p_1, p_2, q_1, q_2): p_1 < -0.3\}$. The escape times are shown in Fig. 3.3 with darker colours indicating short escape times and white representing times exceeding the maximal iteration time. In addition, the 1-tori are included as orange, red and green points like in Fig. 3.2(e).

In the escape time plot Fig. 3.3 one can see a regime of intermediate times roughly between 10^4 and 10^5. The corresponding initial conditions are located close to the island chain. This reminds of escape time plots in 2D maps where the trapping mechanism is understood from partial barriers. Thus, Fig. 3.3 indicates that a similar mechanism holds here, i.e. that there is a partial barrier build by the invariant manifolds of the hyperbolic 1-tori (green). Note that the slight shift of the 1-tori is due to their projection on the plane.

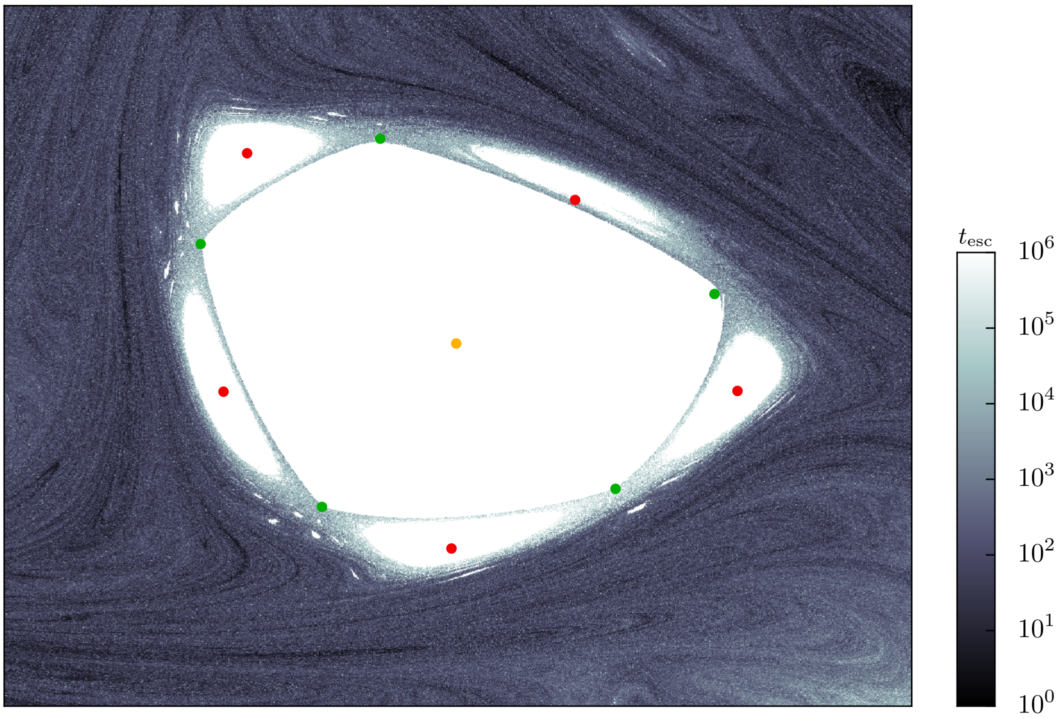

Figure 3.3: Escape time plot for $10^3 \times 10^3$ points started on the plane shown in Fig. 3.2(e), but enlarged by a factor of 1.5. The escape time is encoded as colour with maximal iteration time 10^6 in white. The coloured points are the 1-tori as in Fig. 3.2(e).

4 Turnstile mechanism in 4D maps

In this chapter the analogue of the well known 2D turnstile mechanism, see Sec. 2.1, in a 4D map is discussed. More precisely, we focus on partial barriers composed of stable and unstable manifolds. In a 2D map, the 1D invariant manifolds of hyperbolic fixed points are such a barrier as they have codimension one. In a 4D map, the analogue of a hyperbolic fixed point is a hyperbolic 1-torus with 2D manifolds. However, their dimensionality is insufficient to constitute a barrier in a 4D space. Thus, we have to consider the one-parameter family of 1-tori whose manifolds form a 3D partial barrier separating a resonance zone from the remaining phase space. This can be roughly imagined as a stack of 2D resonances plus a rotation. Hence, also in higher dimensions the turnstile is composed of two lobes, one with the incoming and one with the outgoing points.

Due to crossing resonances there are some missing layers in the stack, i.e. the family of 1-tori is actually a Cantor family with infinitely many gaps. We assume that most of them are too small to have a significant impact on the transport. This is why the gaps are filled by linear interpolation in this thesis. Further details of the construction of the barrier are discussed in Sec. 4.1 using the map $\mathcal{F}$, Eq. (2.2), with parameters $K_1 = 1.8$, $K_2 = 0$ and coupling ξ varying from 0.01 to 0.15 as an example.

With this 3D partial barrier we can survey the turnstile mechanism with the methods explained in Sec. 2.1. On one hand, the transport can be predicted by the enclosed volume of one turnstile lobe, whose computation is shown in Sec. 4.2. On the other hand, the transport across the partial barrier is measured with the point method, which is described in Sec. 4.3. Finally, the results of both approaches are compared, which reveals a very good prediction of the transport in a regime far away from crossing resonances. This is discussed in detail in Sec. 4.4.

4.1 Computation of a 4D turnstile

In order to predict the transport, we need to know the boundaries of the resonance zone and a turnstile lobe as well as their volumes. In this section, we describe the construction of the 4D turnstiles and discuss the related phase space structures.

A 4D volume, e.g. a resonance zone, is bordered by a 3D object. Here, this object is a one-parameter family of 2D manifolds, namely the invariant manifolds of hyperbolic 1-tori. For the construction of a partial barrier all these objects are computed in the following steps:

(i) family of 1-tori, (ii) 2D invariant manifolds (iii) intersections of manifolds (iv) crop manifolds at intersection lines. This leads to the boundary of the transported 4D volume. In addition, we are interested in the (v) local transport, which is studied in terms of sections of the barrier. For all steps this chapter focuses on the results of the computations while numerical details are aggregated in Chap. 5.

(i) The starting point of our computations is the **family of 1-tori**, which can be interpreted as the backbone of the barrier. In the used example map $\mathcal{F}$ the family is stacked along the p_2-coordinate, which leads to a parametrisation of the family by $\hat{p}_2$. The details of the parameter as well as the algorithm to compute 1-tori and its extension to rotational 1-tori is explained in Sec. 5.1. Figure 4.1 shows a projection of all computed 1-tori onto the canonical coordinate planes (q_1, p_1) and (q_2, p_2) for different values of the coupling ξ. Numerically we determine particular members of the family, which results in the small gaps between the tori in the right column. In contrast, the bigger gaps, e.g. close to $p_2 = 0$ or $p_2 = 0.5$, are true gaps of the family. These are the previously mentioned resonance gaps, which occur due to the $|m_N| = 0$ bifurcations explained in Sec. 3.1. In the following, "gaps" refers to resonance gaps unless stated otherwise. With increasing coupling ξ the resonance gaps get bigger and the 1-tori are deformed, as expected. The rising deformation is also visible in the first degree of freedom (left column).

(a) $\xi = 0.01$

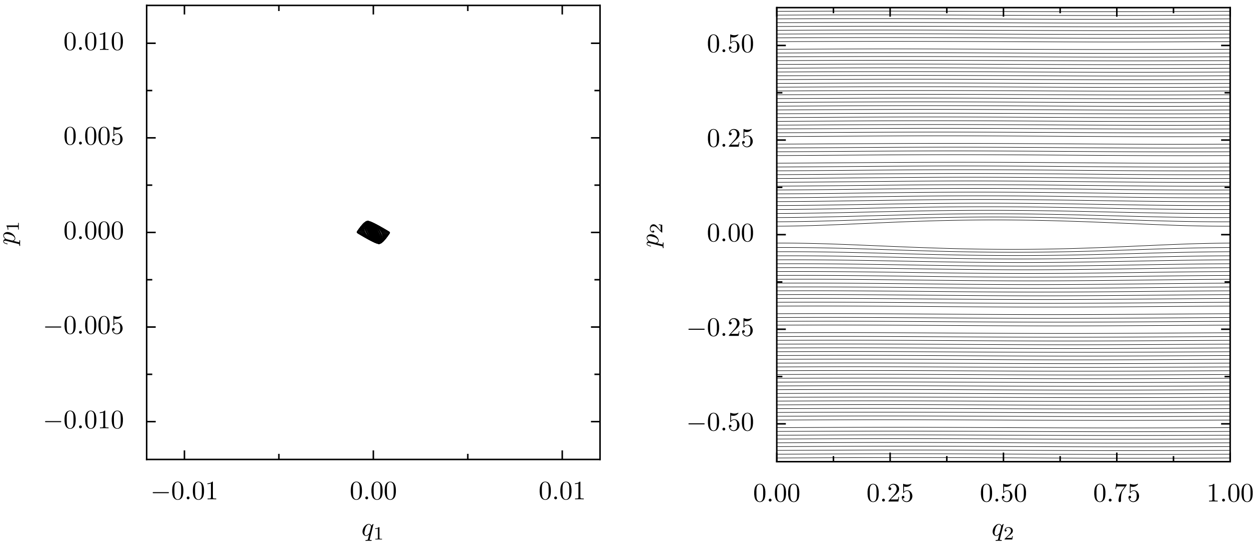

(b) $\xi = 0.1$

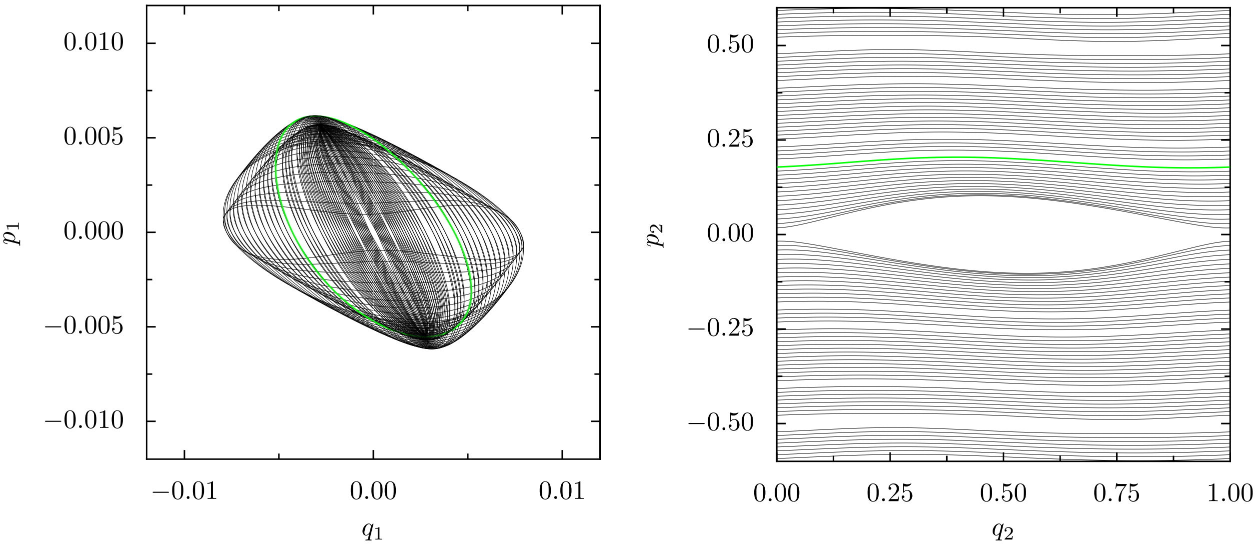

(c) $\xi = 0.15$

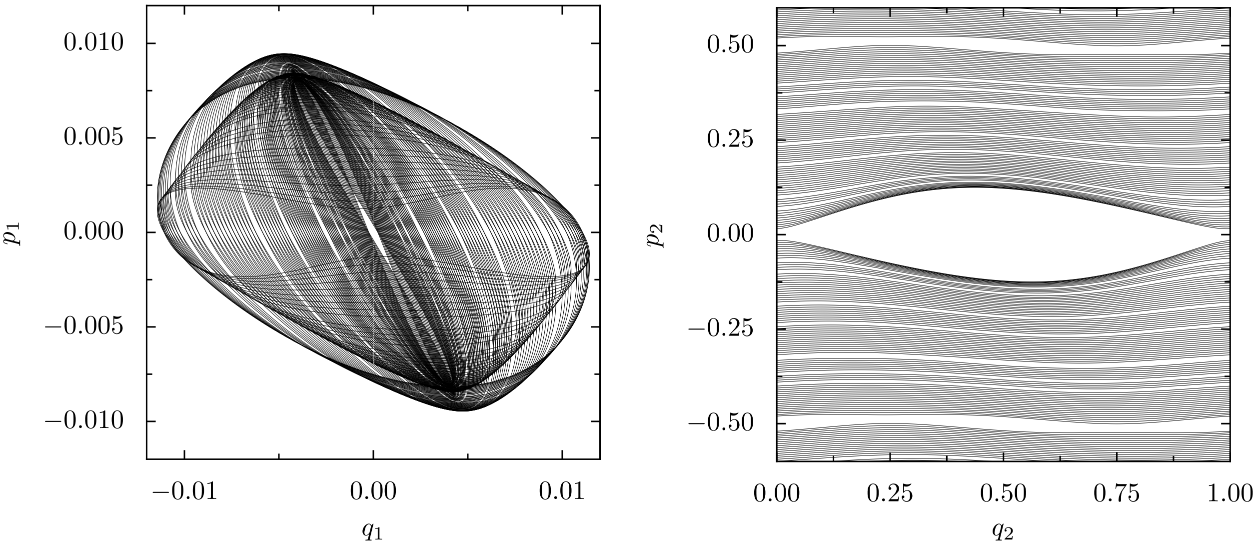

Figure 4.1: Projection of 1-tori to first (left column) and second (right column) degree of freedom for different values of the coupling ξ. The manifolds attached to the green torus in the middle row (b) are shown in Fig. 4.2.

(ii) Each 1-torus has **2D stable and unstable manifolds** attached. The numerical details of their computation are explained in Sec. 5.2.1. As an example Fig. 4.2 shows a single 1-torus with $\hat{p}_2 = \nu = 0.19$ in green and its invariant manifolds in red and blue. More precisely, we see a projection omitting the p_2-coordinate, i.e. only the remaining coordinates (p_1, q_1, q_2) are plotted. The 1-torus is visible twice, because it is located around the periodic boundary in q_1. This is more clear for the green fixed point in the 2D case shown in Fig. 2.1. Also the four attached manifolds resemble the 2D case in the (p_1, q_1)-plane. Hence, there is again an upper $(p_1 > 0)$ and a lower $(p_1 < 0)$ turnstile. The intersection points are more complicated here as two non-parallel 2D manifolds intersect in points in the 4D space. The first intersection points of the stable and the unstable manifold are marked in yellow and the second ones in orange analogue to Fig. 2.1.

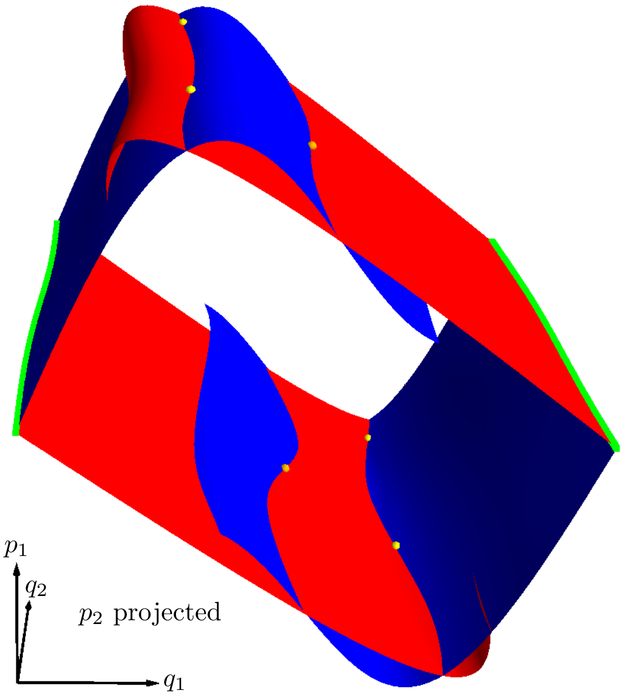

Figure 4.2: Projection of stable (red) and unstable (blue) manifolds of one 1-torus (green) at $\hat{p}_2 = 0.19$ at coupling $\xi = 0.1$, which is marked in Fig. 4.1. The first and second intersection points are shown in yellow and orange, respectively. Note that these are intersection points in all four dimensions, which is not visible here. In the fourth coordinate p_2 the manifolds approximately cover the range $[0.15, 0.23]$. The axes are centred at $(p_1, q_1, q_2) = (-0.5, 0, 0)$.

The manifolds are computed for all 1-tori and look similar for different $\hat{p}_2$. Figure 4.3 shows a section at $q_2 = 0.5$ of the whole family of 1-tori and their manifolds for $\xi = 0.1$. Here, the 1-tori are depicted as dots (green) and the 2D manifolds as red and blue lines. The gaps in the family of 1-tori visible in Fig. 4.1 are resembled as gaps between the manifolds. For a clear view, the manifolds are only shown up to their first intersection points, which are similar to the yellow ones in Fig. 4.2. Note that only the families have to meet in the occurring intersection line, but not every single manifold (lines) has a matching partner. Details on the intersections are explained in part (iii).

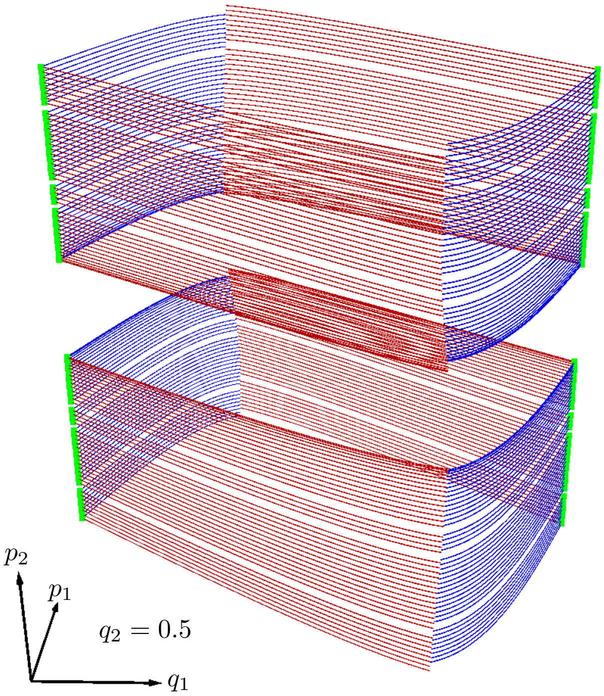

Figure 4.3: Section at $q_2 = 0.5$ of the family of hyperbolic 1-tori (green) and their attached 2D stable (red) and unstable (blue) manifolds. Due to the section all objects appear with a dimension reduced by one. The axes are centred at $(q_1, p_1, p_2) = (0, -0.5, -0.5)$.

In order to save computation time and increase precision in the following steps, we linearly interpolate additional manifolds between the computed ones, see Sec. 5.2.2. In the small discretisation gaps this leads to reasonable additional points whereas in the case of resonance gaps this probably introduces errors. Details and implications of this approach are discussed in Sec. 4.4.

(iii) The next step is the computation of the **intersections** of the families of manifolds, see Sec. 5.2.3 for numerical details and examples. The intersection points of two families of 2D manifolds lie on a 2D surface, which can be understood as follows: Two single 2D manifolds intersect in a 4D space in one or several points, see for an example the yellow points in Fig. 4.2. Hence, every 2D stable or unstable manifold intersects with a one-parameter family of manifolds of opposite stability in a 1D line. Consequently, two families intersect in a 2D surface. The computation of all intersection points is done for the first and second as well as for the upper, i.e. $p_1 > 0$, and the lower, i.e. $p_1 < 0$, intersections.

(iv) The fourth step is to **crop the manifolds**, see Sec. 5.2.4. This is necessary as only a part of the 2D manifolds is relevant for the 3D boundary we are interested in. As an example the unstable manifold of the 1-torus marked in green in Fig. 4.1 is shown in Fig. 4.4 as a projection similar to Fig. 4.2. The part between the green 1-torus and the first intersections (yellow points) with the stable family is shown in darkblue and contributes to the resonance boundary. This is similar to the resonance zone (grey) shown in Fig. 2.1 for the 2D case. Analogously, the part between first (yellow) and second (orange) intersections with the family of stable manifolds belongs to the boundary of one lobe of the turnstile, which is shown in lightblue. The 2D equivalent is the green area A_t in Fig. 2.1. In this way every manifold is cropped at the lines of intersection with the family of manifolds with opposite stability.

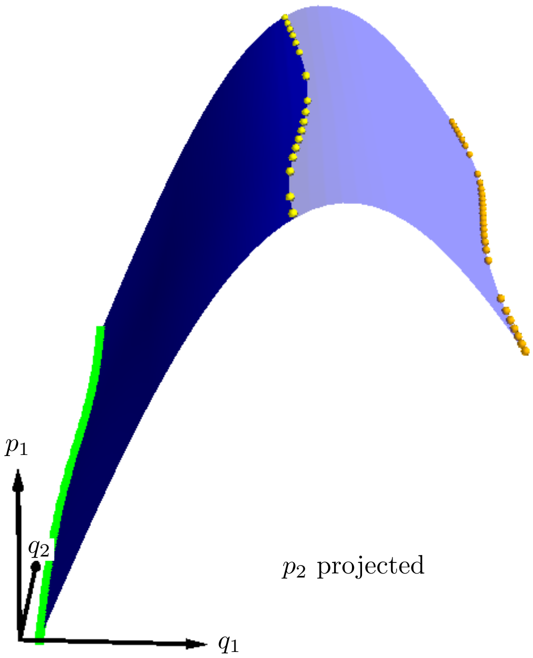

Figure 4.4: Projection of a cropped unstable manifold of the 1-torus (green) marked in Fig. 4.1. The first and second intersections with the family of stable manifolds are shown as yellow and orange points, respectively. The darkblue part up to the first intersections is part of the resonance boundary while the lightblue part between the first and the second intersections belongs to the lobe boundary. The axes are centred at $(p_1, q_1, q_2) = (0, -0.02, 0)$.

Finally, the cropped families of both stable and unstable manifolds build together a 3D barrier in the 4D phase space and hence, enclose a 4D volume. More precisely, the manifold parts from 1-torus to first intersections, e.g. the darkblue one in Fig. 4.4, contribute to the 3D boundary of the 4D resonance zone. The parts between the first and the second intersections like the lightblue one in Fig. 4.4 build the boundary of a turnstile lobe. If there is no additional transport, e.g. for the uncoupled map $\xi = 0$, the sum of the enclosed upper and lower 4D lobe volumes $V^{4\mathrm{D}}_{\mathrm{lobes}} = V^{4\mathrm{D},u}_{\mathrm{lobe}} + V^{4\mathrm{D},l}_{\mathrm{lobe}}$ is transported out of the resonance zone within one iteration step. More precisely, when iterating the phase space volume inside the resonance zone once, the leaving part is mapped to the computed lobes. Since we are dealing with a coupled map $\xi > 0$, there could be additional transport and hence, the value $V^{4\mathrm{D}}_{\mathrm{lobes}}$ is not very meaningful in this case although it is a conserved quantity.

(v) Hence, the more interesting issue is the variation of the turnstile volume along the channel at different positions p_2^*, which we call **local transport**. To this end, we have to find local 2D barriers in 3D subspaces. For this, the 3D barrier is intersected with some 1D condition for the p_2-coordinate

$$\gamma : (q_2, p_2^*) \mapsto p_2. \tag{4.1}$$

In order to get comparable results for every value of p_2^*, the condition should be linear in p_2^*. Due to this requirement and for reasons of clarity and simplicity, we use the condition $p_2 = \gamma(q_2, p_2^*) = p_2^*$. For numerical details of the section see Sec. 5.2.5.

The result of this process is a 2D section of the 3D barrier that exists in the space spanned by the remaining coordinates (p_1, q_1, q_2). As an example the border at $p_2^* = 0.2$ for coupling $\xi = 0.1$ is shown in Fig. 4.5 in black. The cyan points at $q_2 = 0$ serve as a guide to the eye. Note that all points have $p_2 = p_2^* = 0.2$ as fourth coordinate. Thus, this 2D object lives in a 3D space, where it has sufficient dimension to be a barrier.

Note that the enclosed 3D volumes in this decomposition do not necessarily fulfil the same characteristics as the full 4D volume. For instance, the volume of the incoming lobe can differ from the outgoing one as only the integral over the whole channel is a conserved quantity.

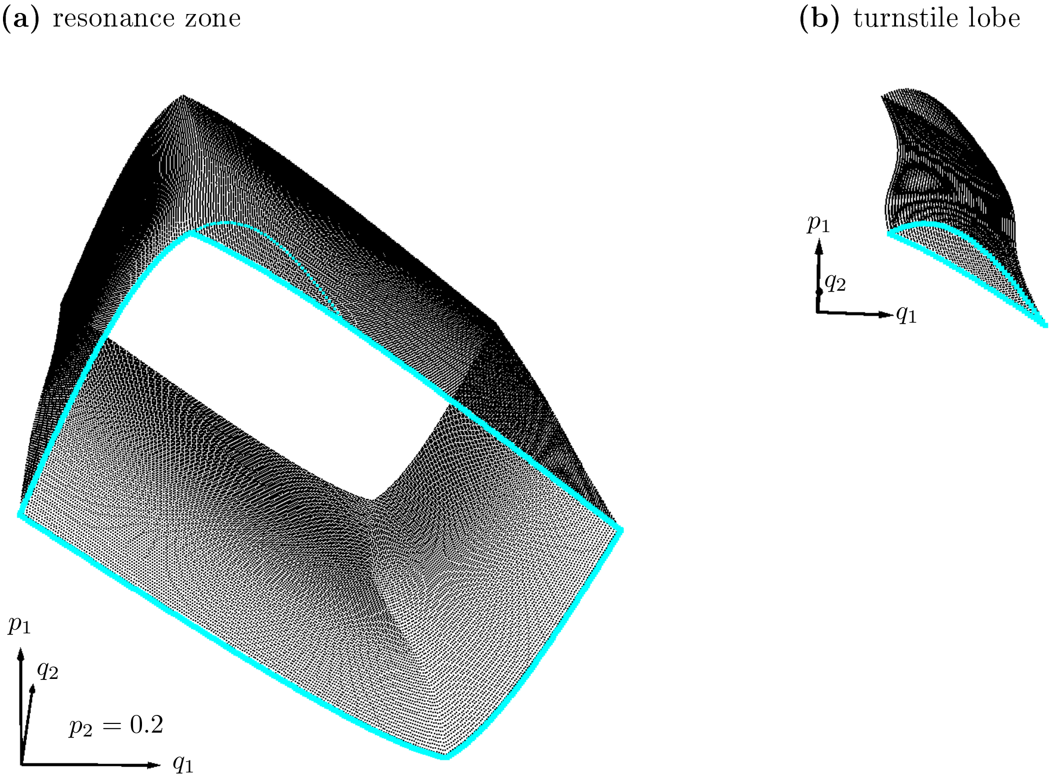

Figure 4.5: 2D section (black) of the 3D barrier at $p_2^* = 0.2$ for coupling $\xi = 0.1$. Points with $q_2 = 0$ are marked in cyan. In (a) the boundary of the resonance zone is shown. Figure (b) displays the boundary of one lobe of the upper turnstile. The cyan points from (b) are also added in (a) as thin line. The axes are centred at $(p_1, q_1, q_2) = (-0.5, 0, 0)$ in (a) and at $(0.35, 0.15, 0)$ in (b).

4.2 Volume measurement

In this section we compute the volumes of the resonance zone and one turnstile lobe enclosed by the boundaries discussed in the previous section 4.1. This leads to a prediction of the transport out of the resonance zone. In particular, we are interested in the variation of the local transport at different positions along the channel. Hence, we focus on the computation of 3D volumes $V^{3\mathrm{D}}$ in the following. The 4D volume $V^{4\mathrm{D}}$ can be simply computed by integration over the parameter p_2^*. The details of the numerical computations corresponding to this section can be found in Sec. 5.3.1.

The 3D volume enclosed by a 2D surface can be computed in various ways. One possibility is the triangulation method described in App. B, but this algorithm is not suited for non-convex surfaces. An easier and more exact option is the decomposition in 2D areas A bordered by 1D lines and subsequently integrating those areas to obtain a 3D volume. For the considered map $\mathcal{F}$ it makes sense to use slices of constant q_2-value, which leads to area computations in the (p_1, q_1) plane very similar to 2D maps, cf. Fig. 2.1. Note that the map $\mathcal{F}$ is periodic in q_2. Thus, the area measured at $q_2 = 0$ has to be equal to the one for $q_2 = 1$.

The results for $p_2^* = 0.2$ serve as an example and are shown in Fig. 4.6 for different couplings ξ. In the first row (a) the computed areas of the resonance zone A_{rz} are plotted as function of q_2. For each value of q_2 the area is comparable to the grey zone in Fig. 2.1. As expected, they vary the more around the uncoupled value (red line) the higher the coupling ξ, but the relative variation is rather small with up to $\approx 2\%$. The second row (b) shows the areas measured in the upper turnstile $A^{\mathrm{u}}_{\mathrm{lobe}}$, which are comparable to the green area A_t in Fig. 2.1. The counterpart of A_t for $p < 0$, i.e. the lower turnstile, is symmetric in the 2D map. However, for the 4D map $\mathcal{F}$ only the reflection of both p-coordinates is a symmetry operation. Hence, for constant p_2^*, there is a difference in the areas of one lobe of the upper $A^{\mathrm{u}}_{\mathrm{lobe}}$ and the lower $A^{\mathrm{l}}_{\mathrm{lobe}}$ turnstile, but they are linked by the full symmetry $A^{\mathrm{l}}_{\mathrm{lobe}}(p_2^*) = A^{\mathrm{u}}_{\mathrm{lobe}}(-p_2^*)$. For comparison with the upper turnstile in Fig. 4.6(b) the lower areas $A^{\mathrm{l}}_{\mathrm{lobe}}$ are shown in the third row (c). There, the variation is rather big, especially for the higher values of ξ in the middle and right column. For $\xi = 0.15$ the area is even close to zero, which is also true for other values of p_2^*. This means that the lines of first and second intersections, exemplarily shown in Fig. 4.4 as yellow and orange points, are no longer collateral. For higher values of ξ they touch and there is no clearly defined turnstile anymore. Hence, our studies are limited to couplings $\xi \leq 0.15$. A similarly vanishing turnstile was observed in a van der Waals complex [76, Ch. 4.1].

(a) Resonance zone

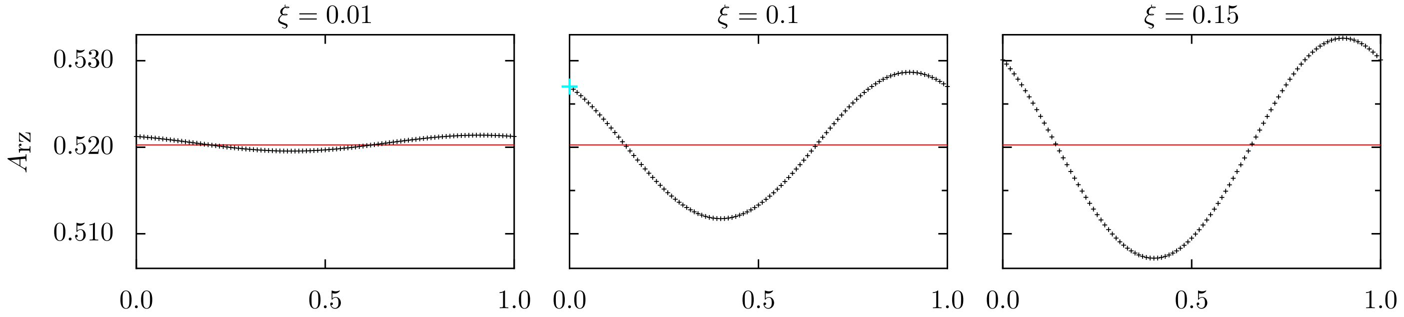

(b) One lobe of upper turnstile

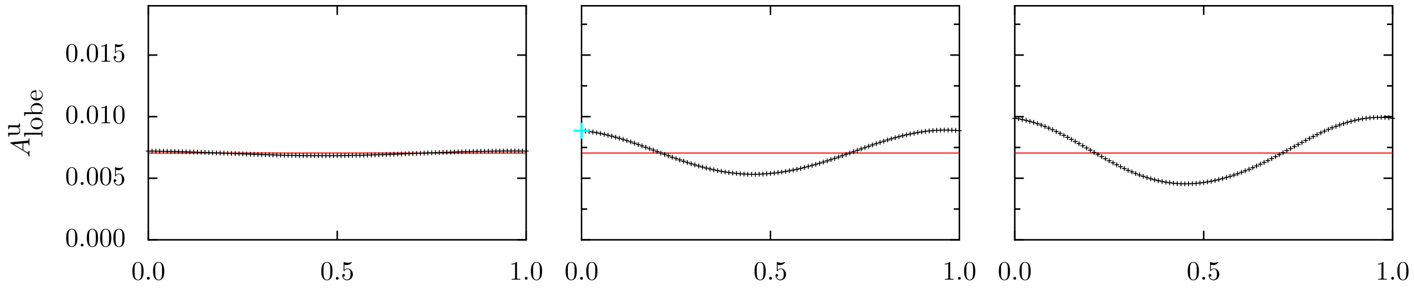

(c) One lobe of lower turnstile

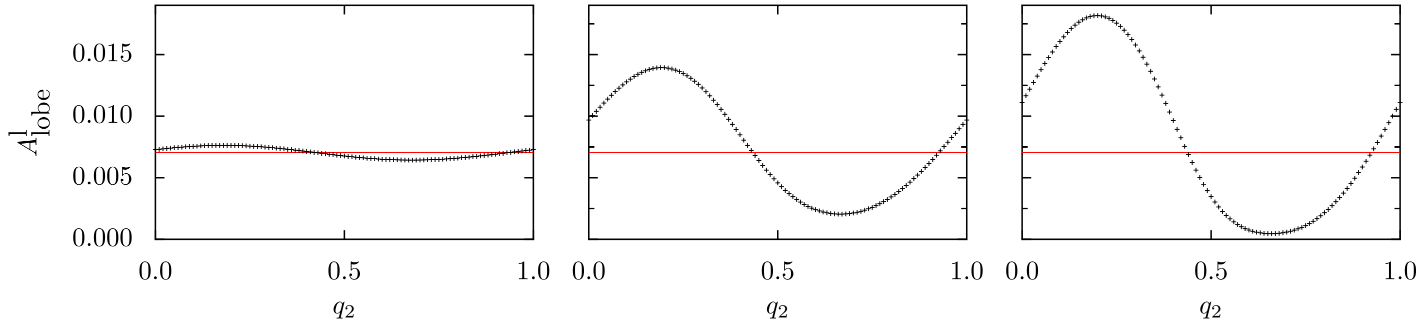

Figure 4.6: 2D areas A at different positions along the q_2-axis for $p_2^* = 0.2$. In all plots the expected area for the uncoupled map is shown as red line. The columns correspond to rising coupling ξ from left to right. The first row (a) displays the area of the resonance zone A_{rz} while (b) and (c) show the area of one lobe of the upper $A^{\mathrm{u}}_{\mathrm{lobe}}$ and lower $A^{\mathrm{l}}_{\mathrm{lobe}}$ turnstile, respectively. In addition, the areas enclosed by the cyan lines in Fig. 4.5 are marked in cyan.

With the 2D areas $A(q_2)$ the 3D volume is calculated $V = \int_0^1 A(q_2)\,\mathrm{d}q_2$. The volume of the resonance zone $V_{\mathrm{rz}}^{3\mathrm{D}}$ is computed from the 2D areas A_{rz} and analogously the upper $V_{\mathrm{lobe}}^{3\mathrm{D},\mathrm{u}}$ and lower $V_{\mathrm{lobe}}^{3\mathrm{D},\mathrm{l}}$ turnstile lobe volumes. Hence, the data shown in one column of Fig. 4.6 leads to one volume for each structure. To study the variation of the volumes along the channel, the areas and the corresponding volumes are computed for all values of p_2^*. Note that the map $\mathcal{F}$ is periodic in p_2 and hence, the volumes at $p_2^* = \pm 0.5$ have to coincide. In addition, the symmetry of the map $\mathcal{F}$ leads to a symmetry of the resonance zone volumes $V_{\mathrm{rz}}^{3\mathrm{D}}(p_2^*) = V_{\mathrm{rz}}^{3\mathrm{D}}(-p_2^*)$ and of the lobe volumes $V_{\mathrm{lobe}}^{3\mathrm{D},\mathrm{l}}(p_2^*) = V_{\mathrm{lobe}}^{3\mathrm{D},\mathrm{u}}(-p_2^*)$, analogue to the areas. As we do not enforce this symmetry, it can serve as a measure for the quality of the data.

The computed volumes are shown in Fig. 4.7 for different couplings. The first row (a) displays the volumes of the resonance zone $V_{\mathrm{rz}}^{3\mathrm{D}}$ with rising coupling ξ from the left to the right column. For $\xi \in \{0.1, 0.15\}$ the volume of the resonance zone is larger in the vicinity of $p_2^* = 0$, which corresponds to a big resonance gap in the family of 1-tori, see Fig. 4.1. In the right plot ($\xi = 0.15$) are some fluctuating points around $p_2^* \approx -0.2$ for some numerical reason. We exclude a physical explanation as the error does not occur for positive p_2^* and we expect a smooth variation.

In the second row (b) are the lobe volumes for the upper $V_{\mathrm{lobe}}^{3\mathrm{D},\mathrm{u}}$ turnstile (dark green) corresponding to Fig. 4.6(b). The volumes of the lower turnstile lobe $V_{\mathrm{lobe}}^{3\mathrm{D},\mathrm{l}}$ are symmetric in p_2^* and were also computed for comparison. The deviation $|V_{\mathrm{lobe}}^{3\mathrm{D},\mathrm{u}}(p_2^*) - V_{\mathrm{lobe}}^{3\mathrm{D},\mathrm{l}}(-p_2^*)|$ is approximately 10^{-6}, which corresponds to a relative error of 0.01%. An exception are the lower volumes for $\xi = 0.15$ at $p_2^* \approx -0.2$ for the same reason as the volumes of the resonance zone in (a).

The third row (c) shows the sum of the two lobe volumes based on the upper lobe volume shown in (b) and the symmetry. This quantity is of interest as this volume is expected to be transported in each iteration step. More precisely, the transport rate r_V across the barrier can be predicted, if there is no additional transport mechanism. The expected rate reads $r_V(p_2^*) = V_{\mathrm{lobes}}^{3\mathrm{D}}(p_2^*)/V_{\mathrm{rz}}^{3\mathrm{D}}(p_2^*)$.

(a) Volume of resonance zone

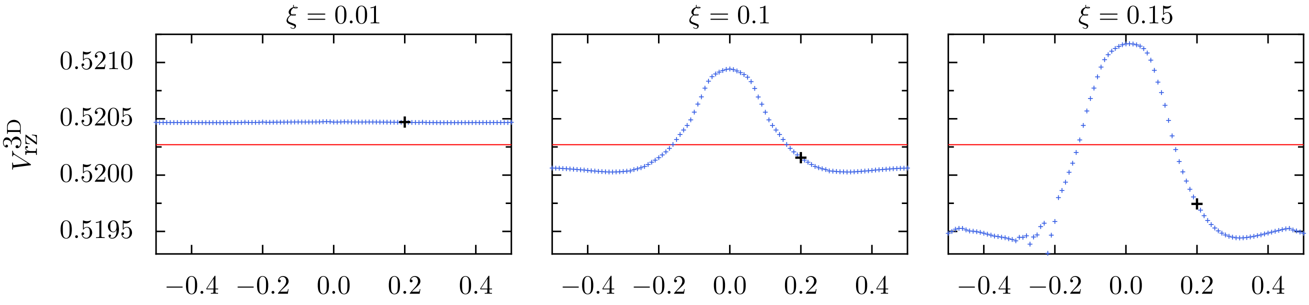

(b) Volume of one lobe of upper turnstile

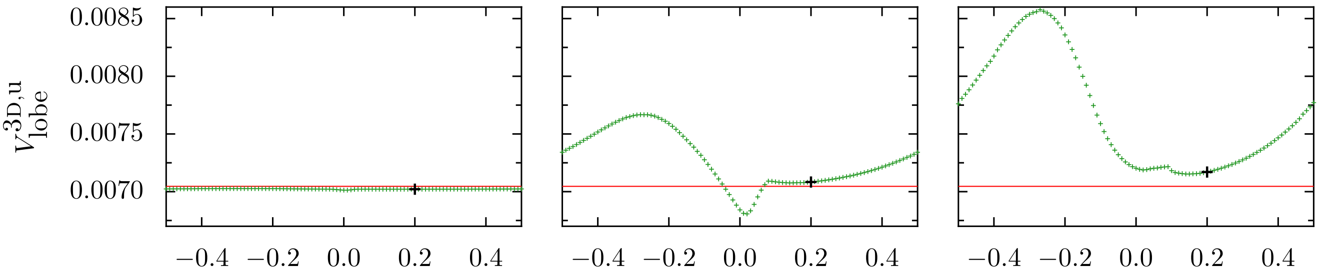

(c) Sum of upper and lower lobe volumes

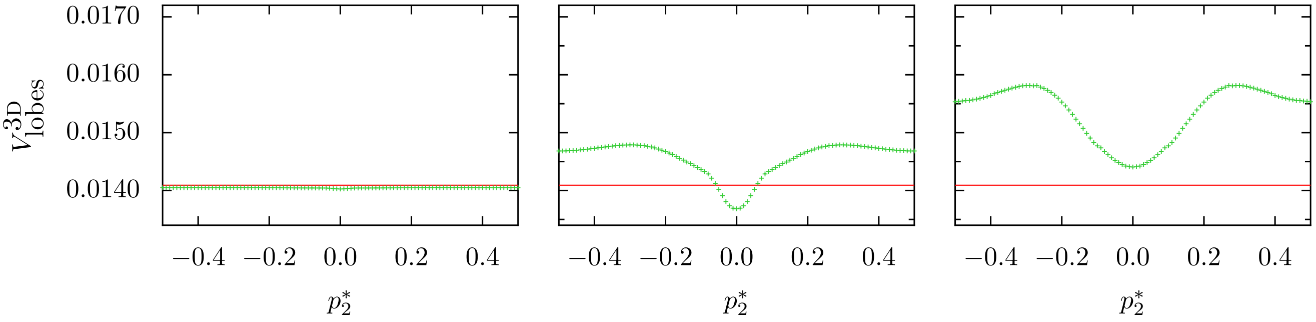

Figure 4.7: 3D volumes as a function of p_2^* along the resonance channel for different couplings ξ. In all plots the expected value for the uncoupled map is shown as red line as in Fig. 4.6. The first row (a) displays the volume of the resonance zone $V_{\mathrm{rz}}^{3\mathrm{D}}$ (blue) while (b) shows the volumes of one lobe of the upper turnstile $V_{\mathrm{lobe}}^{3\mathrm{D,u}}$ in dark green. In addition, the integral over the areas shown in Fig. 4.6(a) and (b) are marked in black in (a) and (b) at $p_2^* = 0.2$, respectively. The last row (c) shows the sum $V_{\mathrm{lobes}}^{3\mathrm{D}}$ of the lobe volumes of the upper and lower turnstile based on the upper lobe and the map symmetry.

4.3 Transport measurement

In this section, we measure transport across the partial barrier constructed in Sec. 4.1. This can be done by starting N_0 uniformly distributed initial conditions inside the resonance zone and counting the remaining N_1 ones after one iteration. With $N_{\text{out}} = N_0 - N_1$ the transport rate then reads $r = N_{\text{out}}/N_0$. The results for the 2D case are given in Sec. 2.1. How to decide numerically whether a point is inside or outside of a 3D boundary in a 4D space is explained in Sec. 5.3.3.

As we are interested in the local transport at a specific position p_2^* of the resonance channel, we start N_0 points in the 3D space spanned by p_1, q_1 and q_2 for each value of p_2^*. How to find these uniformly distributed points inside the resonance zone at constant p_2^* is described in Sec. 5.3.2. Consequently, all points have $p_2 = p_2^*$ and can be iterated with the 4D map. In case of a more general section condition γ, see Eq. (4.1), the p_2-coordinate is set in dependence of the q_2-value. After the iteration step the p_2-coordinate of each point is used to find the most relevant boundary part with the closest p_2^*. This boundary is then used to decide whether the point left the resonance zone or not. If the point is outside, the counter N_{out} corresponding to the p_2^* of the point after the iteration is increased.

Instead of studying the transport rate, one can also investigate the transported phase-space volume. Note that the term *flux* explained in Sec. 2.1 and widely used for 2D maps, is defined as the transported area or, more general, volume in one iteration. As it is usually used for 2D areas and more meaningful for continuous systems, we will rather use the expression *transported volume*. A phase-space volume can be measured with discrete points as follows: If we start N_{g} uniformly distributed points in a phase-space volume V_{ps}, then the volumes of the resonance zone and the transported volume read

$$\tilde{V}_{\text{rz}}^{\text{3D}} = \frac{N_0}{N_{\text{g}}} V_{\text{ps}} \quad \text{and} \quad \tilde{V}_{\text{t}}^{\text{3D}} = \frac{N_{\text{out}}}{N_{\text{g}}} V_{\text{ps}}.$$

Here, the whole 3D phase-space volume $V_{\text{ps}} = 1$ is used, which has the extent $p_1 \in [-0.5, 0.5]$ and $q_1, q_2 \in [0, 1]$ for the map $\mathcal{F}$.

In addition, the points N_{out} found outside the resonance zone after the iteration can be tested to be in the upper lobe N_{u} or the lower lobe N_{l}. To this end, the p_2-coordinate after the iteration is crucial to select the most relevant boundary on one hand and to assign the correct p_2^* on the other hand.

The computed volumes for $N_{\text{g}} \approx 10^7$ initial points are shown in Fig. 4.8 for different couplings ξ. The first row Fig. 4.8(a) displays the volume of the resonance zone $\tilde{V}_{\text{rz}}^{\text{3D}} = N_0/N_{\text{g}}$. The fluctuations visible in the right plot around $p_2^* = -0.2$ are a consequence of the defective boundaries, see Sec. 4.1 and Fig. 4.7(a).

In Fig. 4.8(b) the number of points mapped to the upper turnstile N_{u} is converted to a 3D volume $\tilde{V}_{\text{lobe}}^{\text{3D,u}}$. The curve for the lower turnstile (not shown) is symmetric in p_2^* and includes for $\xi = 0.15$ errors at $p_2^* \approx -0.2$ as a result of the inaccurate boundary as explained before.

The whole volume transported across the barrier $\tilde{V}_{\text{t}}^{\text{3D}} = N_{\text{out}}/N_{\text{g}}$ is shown in the third row Fig. 4.8(c). In case of no additional transport all points get mapped to one of them and hence, $N_{\text{out}} = N_{\text{u}} + N_{\text{l}}$. For $\xi \geq 0.1$ one can guess that $N_{\text{out}} \neq N_{\text{u}} + N_{\text{l}}$, in particular around $p_2^* = 0$. The reason for that is the linear interpolation across the big resonance gap, which is a bad approximation of the partial barrier. More details on this are discussed in the following section 4.4.

(a) Volume based on N_0

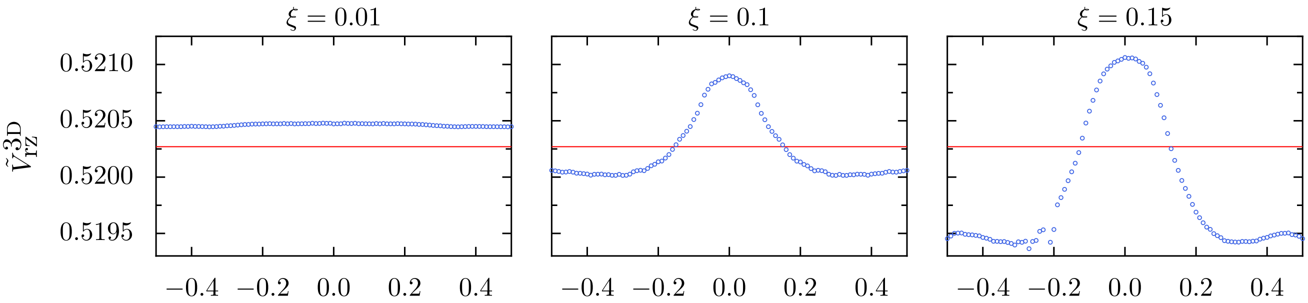

(b) Volume based on N_{u}

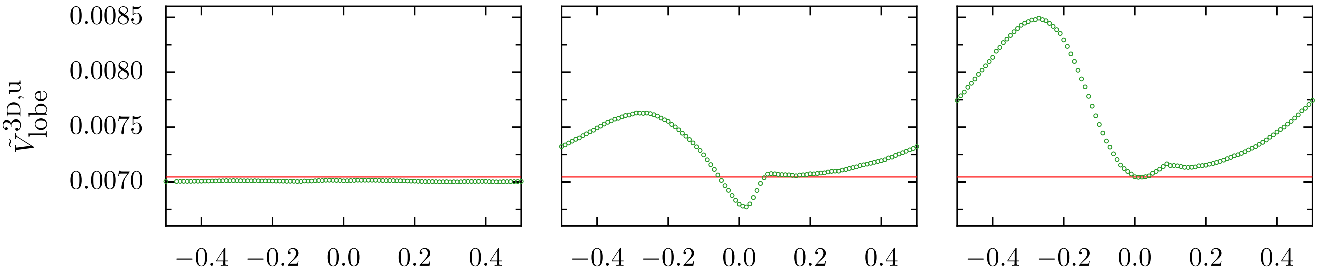

(c) Volume based on N_{out}

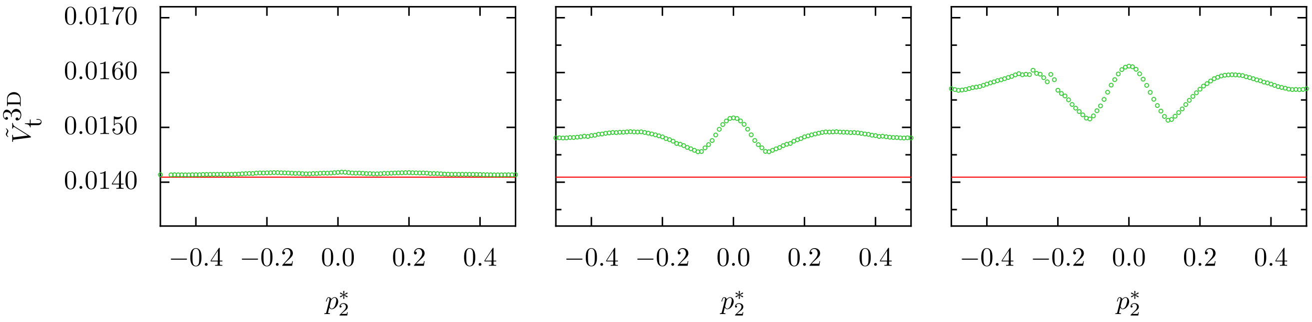

Figure 4.8: 3D volumes along the channel for different couplings ξ. In all plots the expected value for the uncoupled map is shown as red line as before. The first row (a) displays the volume of the resonance zone $\tilde{V}_{\text{rz}}^{\text{3D}}$ (blue) while (b) shows the volumes of one lobe of the upper turnstile $\tilde{V}_{\text{lobe}}^{\text{3D,u}}$ in dark green. The last row (c) visualises the transported volume $\tilde{V}_{\text{t}}^{\text{3D}}$ in green.

4.4 Comparison of volumes and transport

In the previous sections two methods to study transport across a partial barrier in a 4D phase space are discussed. The first one in Sec. 4.2 computes turnstile lobe volumes via an integration over enclosed areas while the second one in Sec. 4.3 measures the transported volume based on the one-step dynamics of an ensemble of many initial conditions. We call these methods the volume and the point method, respectively. As long as there is no transport additional to the turnstile mechanism, the volumes predict the number of transported initial conditions apart from numerical errors. This is expected to be the case far away from major resonance crossings. In contrast, in resonance gaps the linearly interpolated barrier probably provides no reasonable prediction of the transport. Hence, we expect a difference between the two measurements at crossing resonances, especially around the most relevant one at $p_2 = 0$.

The results of the volume and the point method shown before in Figs. 4.7 and 4.8 are merged in Fig. 4.9. The first part Fig. 4.9(a) shows the volume of the resonance zone, for which both methods should yield the same as no transport is involved. Hence, deviations are due to systematic and numerical errors. For most p_2^*-values the error is $\approx 3 \cdot 10^{-5}$, which is even less than in the 2D case, see Sec. 2.1 for comparison. The largest deviations are visible around $p_2^* = 0$ for $\xi \in \{0.1, 0.15\}$. For $\xi = 0.15$ the maximal error is $\approx 10^{-4}$, which corresponds to a relative error of 0.02%. Although this is a very small deviation it remains unclear why it is larger around $p_2^* = 0$ than in other domains. Note that the fluctuating points around $p_2^* = -0.2$ are due to the inaccurate boundary for these parameters, see Sec. 4.2.

If the transport is ruled mainly by the turnstile mechanism, the points mapped outside are expected to be found in a turnstile lobe. To test this, Fig. 4.9(b) shows the upper turnstile lobe volumes (+) and the number of initial points (○) mapped into them for different couplings ξ. Note that the data for the lower turnstile was also computed and is symmetric apart from fluctuating points around $p_2^* = -0.2$ for $\xi = 0.15$, which are due to the inaccurate boundary for these parameters. The black line is based on a different approach involving a NHIM, which is explained in more detail below. Overall, the volume method and the point method are in very good agreement. For $\xi = 0.1$ in the second row of Fig. 4.9(b) even in the vicinity of the crossing resonance the deviations are small with up to $5 \cdot 10^{-5}$. This is comparable to the 2D experiment with errors of $\approx 4.8 \cdot 10^{-5}$ and in the range of the expected statistical error of $5.5 \cdot 10^{-5}$. In the third row, for $\xi = 0.15$, the errors range from $1.5 \cdot 10^{-5}$ to $1.5 \cdot 10^{-4}$ at $p_2^* = 0$. In addition to this expected divergence due to the resonance gap, there is a deviation around $p_2^* = -0.29$, which is due to numerical difficulties.

Finally, Fig. 4.9(c) shows the predicted transport (+) and the volume corresponding to the number of points mapped outside (○), i.e. the transported volume. As expected, the rough approximation of the barrier in the large resonance gap leads to strong deviations of $\approx 1.7 \cdot 10^{-3}$ around $p_2^* = 0$ for $\xi \in \{0.1, 0.15\}$. The fluctuating points around $p_2^* = -0.2$ for $\xi = 0.15$ are due to the inaccurate boundary for these parameters, see Sec. 4.2. Apart from the crossing resonance and these fluctuations there are errors of approximately $1.5 \cdot 10^{-4}$ corresponding to $\approx 1\%$, which is above the expected statistical error of $7.7 \cdot 10^{-5}$. Considering the high number of computational steps that include interpolations, the curves are in very good agreement. Hence, we conclude that the transport is dominated by the turnstile mechanism in a regime far away from crossing resonances.

There are multiple ways to reduce the numerical errors and to find better approximations of the partial barrier in resonance gaps. For instance, one could replace the linear interpolation by a polynomial one or a Fourier-expansion. Furthermore, the rotational hyperbolic 1-tori inside the resonance gap could serve as additional sampling points. Also the linear interpolations of the stable and unstable manifolds, between the intersection points and of the borders for the area computations could be replaced by more exact ones.

A completely different approach not followed in this thesis is to directly consider a NHIM instead of the family of hyperbolic 1-tori living on the NHIM. The main advantage of this approach is that a NHIM is clearly defined and computable over the whole extent, i.e. also where the family has gaps. Consistently with the invariant manifolds of the 1-tori, the NHIM has attached 3D invariant manifolds that intersect in 2D manifolds. These intersection manifolds can be numerically determined with a 2D bisection algorithm in (p_1, q_1) for each value of the (p_2, q_2)-coordinates [77], similar to the method in Ref. [72] described in Sec. 2.4. This was implemented by R. Ketzmerick for the first and the second intersection of the invariant manifolds. Additionally, the stable and unstable manifolds between the intersections can be computed with a 1D bisection in p_1 for various q_1. This yields the border of a turnstile lobe, whose enclosed volume is determined based on a Chebyshev approximation [77]. The outlined method is considered to be very accurate.

The result for the upper turnstile is shown as black line in Fig. 4.9(b) for $\xi \in \{0.1, 0.15\}$. In comparison with the volume method (+) described in Sec. 4.2 the deviations are $\approx 3 \cdot 10^{-5}$ apart from the resonance at $p_2^* = 0$. This proves that indeed both approaches lead to the same physical structure and, hence, the same prediction for the transport, which can also be seen in Fig. 4.9(c). There, the black line is the sum of upper and lower turnstile volume computed from the upper value and the map symmetry.

Note that it does not make sense to compare results of the point method from Sec. 4.3 with the NHIM approach in detail, because the initial points are already based on the boundaries computed from the 1-tori and their attached manifolds. For a complete discussion, the initial points have to be chosen inside the partial barrier based on the NHIMs. This leads to excellent agreement for all values of p_2^* (not shown) [77]. Thus, the turnstile mechanism can be extended to partial barriers in 4D systems consisting of the 3D invariant manifolds of 2D NHIMs.

(a) Volume of resonance zone $V_{\mathrm{rz}}^{3\mathrm{D}}$ and of N_0 points $\tilde{V}_{\mathrm{rz}}^{3\mathrm{D}}$

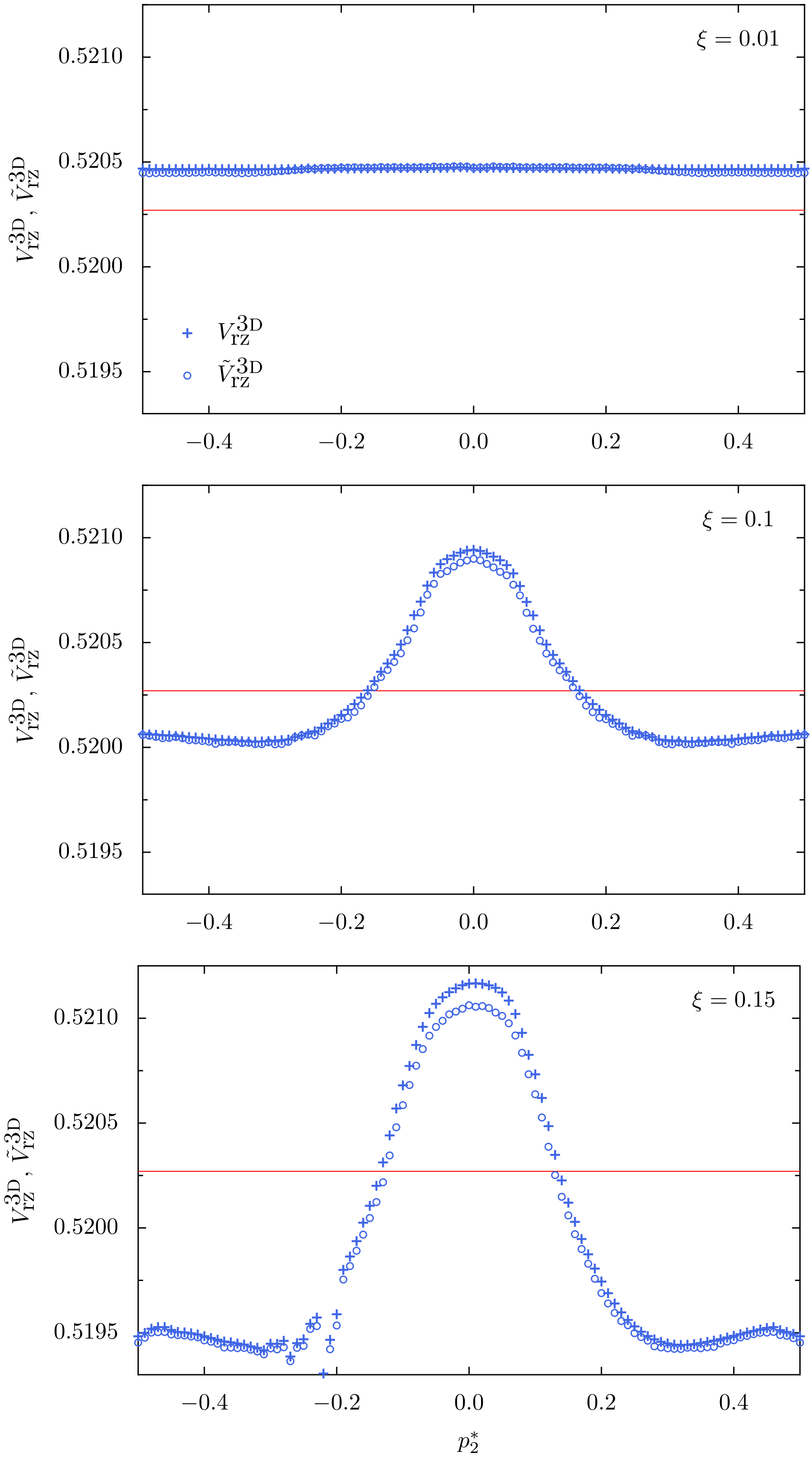

(b) Volume of upper turnstile lobe $V^{3\text{D},\text{u}}_{\text{lobe}}$ and volume of points mapped into the upper lobe $\tilde{V}^{3\text{D},\text{u}}_{\text{lobe}}$

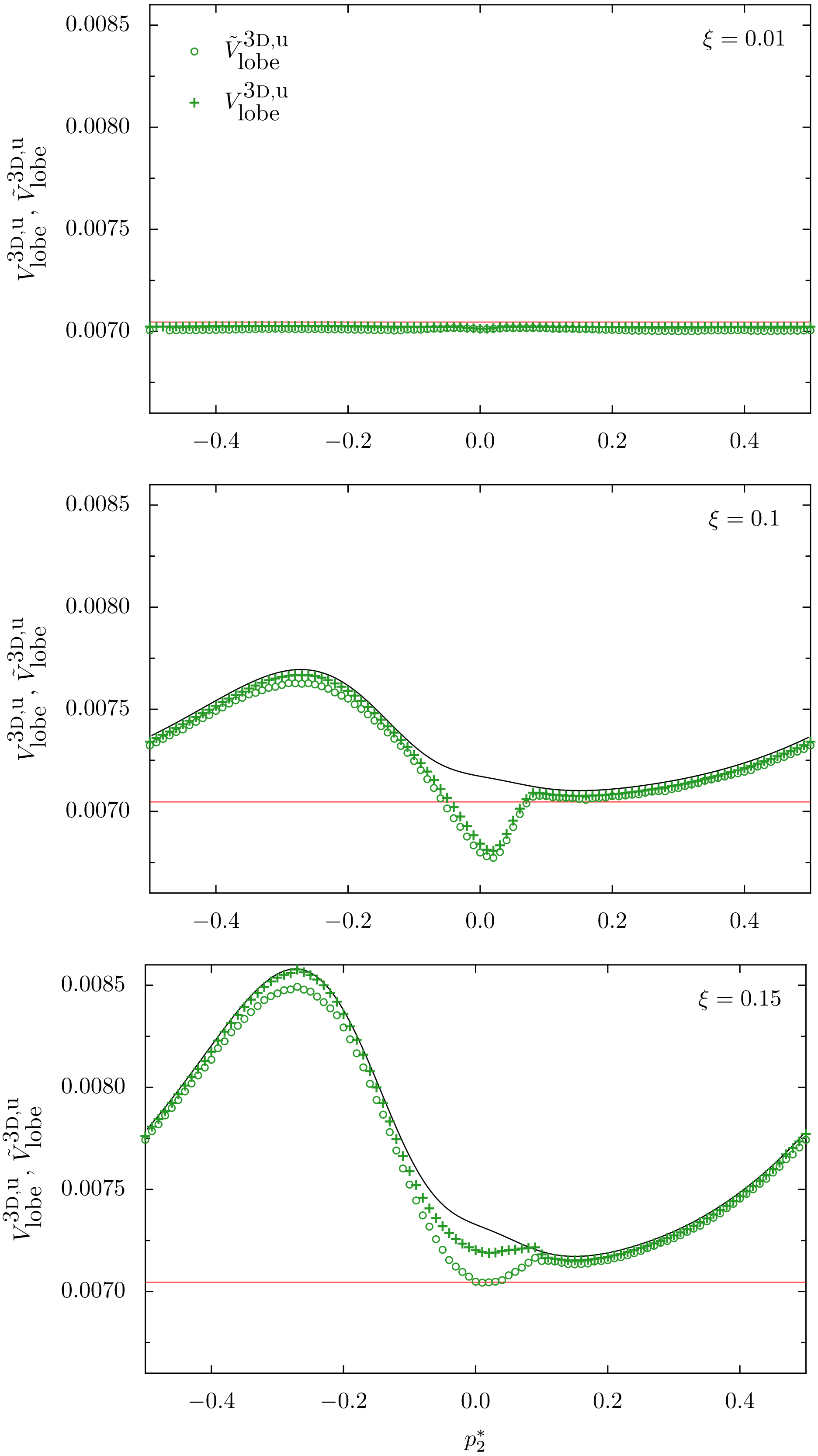

(c) Total lobe volume $V^{3\text{D}}_{\text{lobes}}$ and total transported volume $\tilde{V}^{3\text{D}}_{\text{t}}$

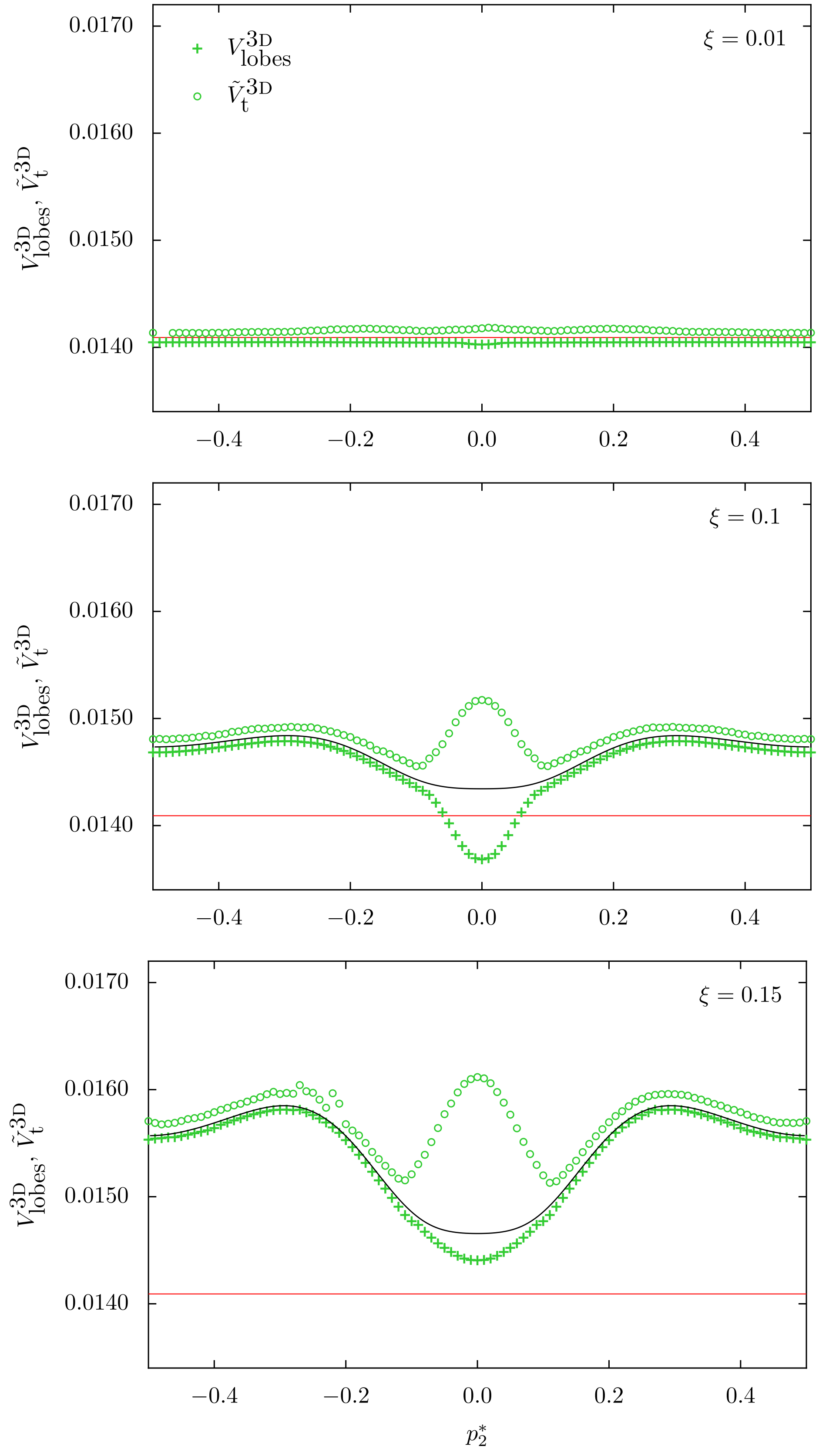

Figure 4.9: Comparison of volumes $V^{3\text{D}}$ based on computed areas (+) and on point numbers $\tilde{V}^{3\text{D}}$ (○) as shown in Fig. 4.7 and Fig. 4.8, respectively. In all plots the expected value for the uncoupled map is shown as red line as before. The black line is based on the NHIM approach [77]. The rows of each subplot correspond to different values of the coupling ξ.

5 Numerical methods

This chapter collects all the numerical details omitted in the previous chapter 4. The first section 5.1 explains the computation of 1-tori for the rotational topology and describes how to obtain an appropriate initial guess. The section 5.2 deals with the invariant manifolds, namely how to compute, interpolate, intersect and crop them. In addition, the section of a 3D barrier in a 4D space leading to a 2D barrier in a 3D space is explained. The last part Sec. 5.3 discusses computations in the resulting 3D space.

5.1 Computation of 1-tori

In previous works [46,75] we used an algorithm from Jorba et al. [64,78] to compute hyperbolic 1-tori. The basic idea is to describe a 1-torus with a longitudinal frequency ν by a truncated Fourier series with N coefficients a_k, b_k:

$$x(\theta) = a_0 + \sum_{k=1}^{N} a_k \cos(k\theta) + \sum_{k=1}^{N} b_k \sin(k\theta),$$

where $\theta \in \mathbb{T} = [0, 2\pi)$, $a_k, b_k \in \mathbb{R}^4$. This method requires topologically closed curves, i.e. librational tori. Due to the small coupling we are dealing with rotational tori, see Sec. 4.1. In order to use the same algorithm a suitable transformation has to be applied.

5.1.1 Transformation

In the following, a 2D transformation is discussed, because not all degrees of freedom need to be adapted. For example, in the map $\mathcal{F}$ only the second degree of freedom is affected, cf. Fig. 4.1.

The algorithm from Jorba operates in the transformed space $(\tilde{p}, \tilde{q}) \in \mathbb{R}^2$ while the original phase-space coordinates $(p, q) \in ([-0.5, 0.5], [0, 1])$ are needed to iterate points with some map M. Hence, a transformation $T\colon (\tilde{p}, \tilde{q}) \mapsto (p, q)$ is necessary before a map $M(p, q)$ can be applied. After the iteration, the point is transformed back by T^{-1}. That is, the algorithm is executed with the map $T^{-1} \circ M \circ T$.

In addition to the mapping the algorithm uses the linearised map $DM(p,q)$. There, the transformation can be included using the chain rule leading to

$$D(T^{-1} \circ M \circ T)(\tilde{p},\tilde{q}) = DT^{-1}(M(p,q)) \cdot DM(p,q) \cdot DT(\tilde{p},\tilde{q}). \tag{5.1}$$

Hence, in addition to T and its inverse T^{-1}, its linearisation DT and the linearisation of the inverse DT^{-1} are involved.

The data shown in Chap. 4 was generated with a transformation that interprets the coordinates of a rotational torus (p,q) as polar coordinates (r,α). An illustration is shown in Fig. 5.1. The transformation T turning Cartesian into polar coordinates is

$$T(\tilde{p},\tilde{q}) = \begin{pmatrix} p \equiv r \\ q \equiv \alpha \end{pmatrix} = \begin{pmatrix} \sqrt{\tilde{p}^2+\tilde{q}^2} \\ \frac{1}{2\pi}\operatorname{arctan2}(\tilde{p},\tilde{q}) \end{pmatrix}.$$

Note that the transformation T is not symplectic as this property is not necessary here.

Its linearisation DT reads

$$DT(\tilde{p},\tilde{q}) = \begin{pmatrix} \frac{\tilde{p}}{\sqrt{\tilde{p}^2+\tilde{q}^2}} & \frac{\tilde{q}}{2\pi(\tilde{p}^2+\tilde{q}^2)} \\ \frac{\tilde{q}}{\sqrt{\tilde{p}^2+\tilde{q}^2}} & -\frac{\tilde{p}}{2\pi(\tilde{p}^2+\tilde{q}^2)} \end{pmatrix}. \tag{5.2}$$

Analogously, the inverse transformation T^{-1} is

$$T^{-1}(p,q) = \begin{pmatrix} \tilde{p} \\ \tilde{q} \end{pmatrix} = \begin{pmatrix} p\sin(2\pi q) \\ p\cos(2\pi q) \end{pmatrix}$$

and its linearisation DT^{-1} reads

$$DT^{-1}(p,q) = \begin{pmatrix} \sin(2\pi q) & \cos(2\pi q) \\ 2\pi p\cos(2\pi q) & -2\pi p\sin(2\pi q) \end{pmatrix}.$$

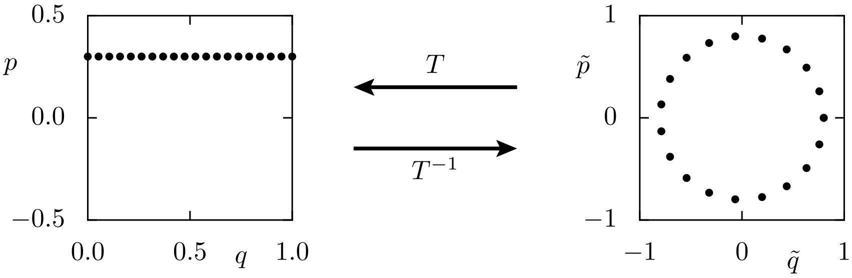

Figure 5.1: Sketch of transformation T including a shift $s = 0.5$ between phase space (p,q) and the transformed space $(\tilde{p},\tilde{q})$.

Polar coordinates require a positive radius, i.e. $p > 0$. But, as mentioned above, p can be negative for the map $\mathcal{F}$. This is solved by adding a shift s, e.g. $s = 0.5$, to the p-coordinate, which leads to the following version of the transformation

$$T(\tilde{p}, \tilde{q}) = (p, q) = \begin{pmatrix} \sqrt{\tilde{p}^2 + \tilde{q}^2} - s \\ \frac{1}{2\pi} \arctan 2(\tilde{p}, \tilde{q}) \end{pmatrix}, \tag{5.3}$$

its inverse

$$T^{-1}(p = r, q = \alpha) = (\tilde{p}, \tilde{q}) = \begin{pmatrix} (p + s)\sin(2\pi q) \\ (p + s)\cos(2\pi q) \end{pmatrix} \tag{5.4}$$

and the inverse linearisation

$$DT^{-1}(p, q) = \begin{pmatrix} \sin(2\pi q) & \cos(2\pi q) \\ 2\pi(p + s)\cos(2\pi q) & -2\pi(p + s)\sin(2\pi q) \end{pmatrix}. \tag{5.5}$$

The linearisation DT is not affected by the shift.

5.1.2 Initial guess for computation

In order to find the hyperbolic 1-tori, the algorithm mentioned above needs an initial guess for the longitudinal frequency ν and for the coefficients a_k, b_k that describe the torus in Fourier space. For a very detailed explanation of the algorithm and other ways to find initial guesses see Ref. [75, Sec. 3.2].

In the uncoupled map, i.e. $\xi = 0$, the frequency ν of a 1-torus corresponds to its p_2-value. As frequencies are only defined up to unimodular transformations, we consider $\nu = |p_2|$. In order to find the family of 1-tori, we choose evenly distributed frequencies. Note that for $\xi > 0$ the corresponding 1-tori are not necessarily equidistant in phase space, which can be seen for instance around $p_2 = 0$ in Fig. 4.1(c).

For each frequency also an initial guess for the Fourier coefficients describing the 1-torus is necessary. The initial guesses used in this thesis are based on three different approaches. The first one is to use the known 1-tori of the uncoupled map. This works the better the smaller the coupling. Analogously, the second approach is based on the results for a smaller coupling. Thirdly, a continuation along the family in p_2-direction can be utilised especially for higher couplings. That is, the Fourier coefficients are extrapolated from already known 1-tori at the same coupling ξ.

In the following, the family of 1-tori is parametrized with the frequency ν for positive p_2 and with $-\nu$ for negative p_2. For simplicity, this parameter will be called $\hat{p}_2$. The step size in $\hat{p}_2$ along the family is $\Delta\hat{p}_2 = 10^{-2}$ for $\xi \in \{0.01, 0.1\}$ and $\Delta\hat{p}_2 = 5 \cdot 10^{-3}$ for $\xi = 0.15$.

5.2 Computation and manipulation of manifolds

With the hyperbolic 1-tori at hand, the next step is to compute their stable and unstable invariant manifolds, which is described in Sec. 5.2.1. Because this is a numerically cumbersome step, additional manifolds are interpolated in between the computed ones like explained in Sec. 5.2.2. All of them are then intersected with each other, see Sec. 5.2.3, and cropped along the intersection lines, see Sec. 5.2.4. Finally, sections of the whole family of manifolds are computed as explained in Sec. 5.2.5.

5.2.1 Computation of invariant manifolds

The algorithm used to compute the invariant manifolds was suggested in Ref. [64, Sec. 5.3.2]. A detailed review of the computation of the normal behaviour of a 1-torus can be found in Ref. [75, Sec. 3.3].

Basically, the normal behaviour at each angle θ along the 1-torus is described by the operator $T_{-2\pi\nu} \circ A(\theta)$, where T is a translation and A the derivative of the map in Fourier space. While we focus on the eigenvalues of this operator in Ref. [75], the corresponding eigenvectors $\psi(\theta)$ are of interest here. They describe the linear direction of the invariant manifolds at each point $x(\theta)$ of the hyperbolic 1-torus. In order to grow the manifolds with map iterations we start n_p equidistant points on the vector $x(\theta) + h\psi(\theta)$ scaled by a small factor h for n_θ values of θ. This is illustrated by a sketch in Fig. 5.2. The 1-torus is depicted as green circle in the middle surrounded by the linearised stable manifold (red). The region is scaled to the width h and filled with $n_\theta = 10$ (angular direction) times $n_p = 5$ (radial direction) grey points. These points are iterated either forward, in case of the unstable manifold, or backward for the stable one. After one iteration the points build rings parallel to the 1-torus, but they are no longer uniformly distributed in angular direction. This is indicated by the middle ring of black dots. In order to prevent a highly non-uniform distribution of points on the manifolds, this is corrected based on a Fourier transformation of the mapped points. More precisely, the resulting Fourier series is evaluated at n_θ angles. The in this way recomputed points are shown in red in Fig. 5.2 and distributed uniformly on the ring. This is repeated for n_s iterations, the sketch depicts $n_s = 2$ steps. For the results shown in Chap. 4 the following parameter values are used: $n_\theta = 2048$, $h = 10^{-4}$, $n_p = 50$ (for $\xi \in \{0.01, 0.1\}$), $n_p = 60$ (for $\xi = 0.15$) and $n_s = 9$.

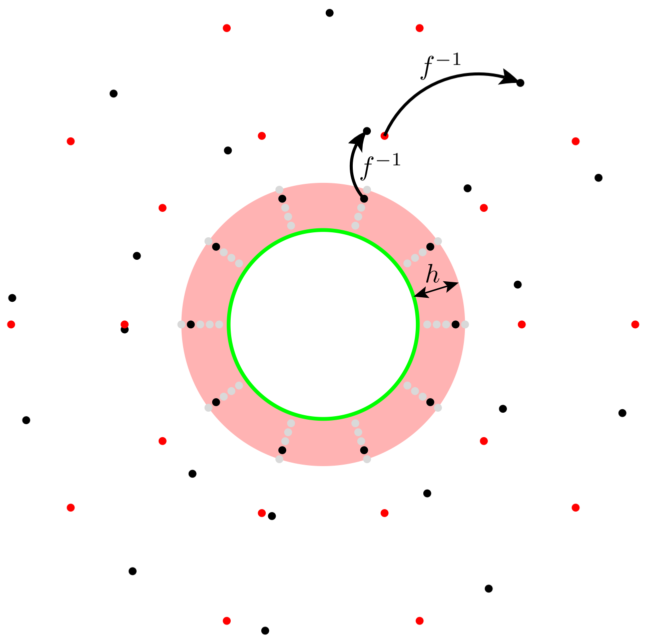

Figure 5.2: Sketch of the growing process. The green line represents the 1-torus and the red region of width h marks its linearised stable manifold. For details on the black and red points see text.

5.2.2 Interpolation of invariant manifolds

The interpolation of additional manifolds leads to a higher density of manifolds in $\hat{p}_2$ and thus, to a higher accuracy of the final results. In addition, this step can replace manifolds with a failed growing or cropping process, see Sec. 5.2.4.

Each point on a manifold can be parametrized by the angle θ and the iteration step s. Furthermore, along the family each manifold is characterized by the parameter $\hat{p}_2$ of the corresponding 1-torus. These three coordinates define a regular grid, in which each parameter point $(\theta, s, \hat{p}_2)$ decodes a point (p_1, p_2, q_1, q_2) in the 4D phase space. To linearly interpolate parameter points on a finer grid in $\hat{p}_2$ direction, we utilize the standard method `interpn` from the interpolate subpackage of SciPy [79]. This way the distance in $\hat{p}_2$ is reduced to $\Delta\hat{p}_2 = 10^{-3}$ over the whole range $\hat{p}_2 \in [-0.5, 0.5]$. Remember that the 1-tori are computed with a density of $\Delta\hat{p}_2 = 10^{-2}$ for $\xi \in \{0.01, 0.1\}$ and $\Delta\hat{p}_2 = 5 \cdot 10^{-3}$ for $\xi = 0.15$. In addition, there are gaps in the family of 1-tori due to resonances. Both, the discretization gaps and the resonance gaps are filled by interpolated manifolds.

5.2.3 Computation of intersections

The task of finding the 2D intersection of two families of stable and unstable manifolds can be solved by the repeated computation of intersection points of two single manifolds. They are found by the full-dimensional root search `fsolve` from the optimize subpackage of SciPy [79]. The function to find roots for is the difference vector

$$d(q_{2,1}, q_{2,2}, m_1, m_2) = x_1(q_{2,1}, m_1) - x_2(q_{2,2}, m_2) \overset{!}{=} 0$$

between points $x_1, x_2 \in \mathbb{R}^4$ on the manifolds, which are parametrised by the q_2-coordinate and the index $m \in [0, n_p \cdot n_s]$ in the growing direction. In order to evaluate the function d at arbitrary parameter values, the manifolds are interpolated linearly in between the discrete points describing them as explained in the previous sections. The initial guesses for the parameters are then chosen such that the first and second intersections are found. As an example the upper and lower homoclinic intersection points of the manifolds of one 1-torus are shown in Fig. 4.2 as yellow and orange points.

This procedure is done for the upper and lower intersections of each member of the stable family with each member of the unstable family along $\hat{p}_2$. The resulting upper intersection points are shown in Fig. 5.3 as a projection to the (p_2, q_2)-plane for different couplings ξ. The left column depicts the first intersection points and the right column the second ones. As with rising ξ from (a) to (c) the manifolds are deformed more heavily, the density of intersection points increases. The colour of the points encodes $\hat{p}_2$ of the involved stable manifold, i.e. a line of constant colour corresponds to one stable manifold.

The lower intersections are arranged symmetrically to the upper ones under negation of all coordinates, which arises from symmetries of the map $\mathcal{F}$. A colouring based on $\hat{p}_2$ of the unstable manifold looks similar.

(a) $\xi = 0.01$

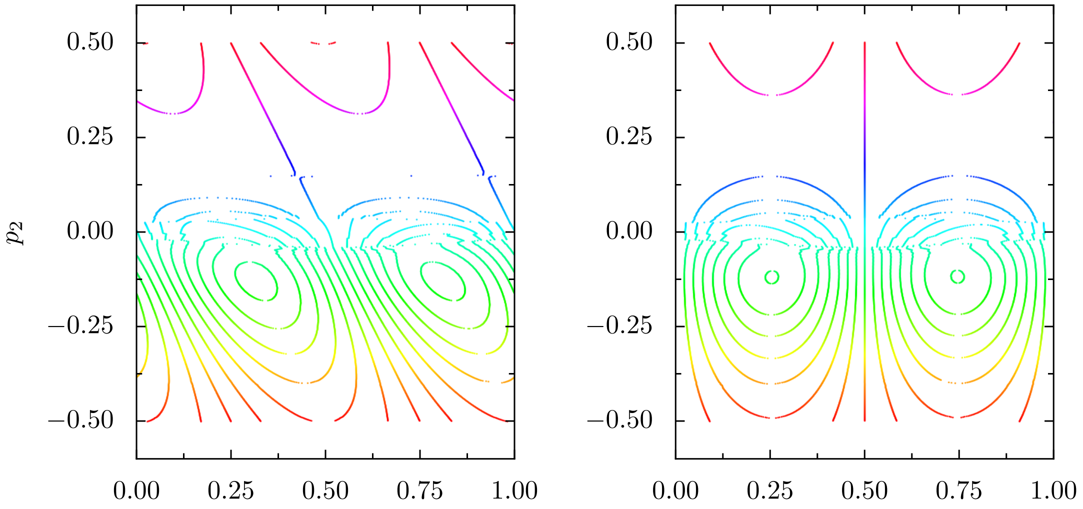

(b) $\xi = 0.1$

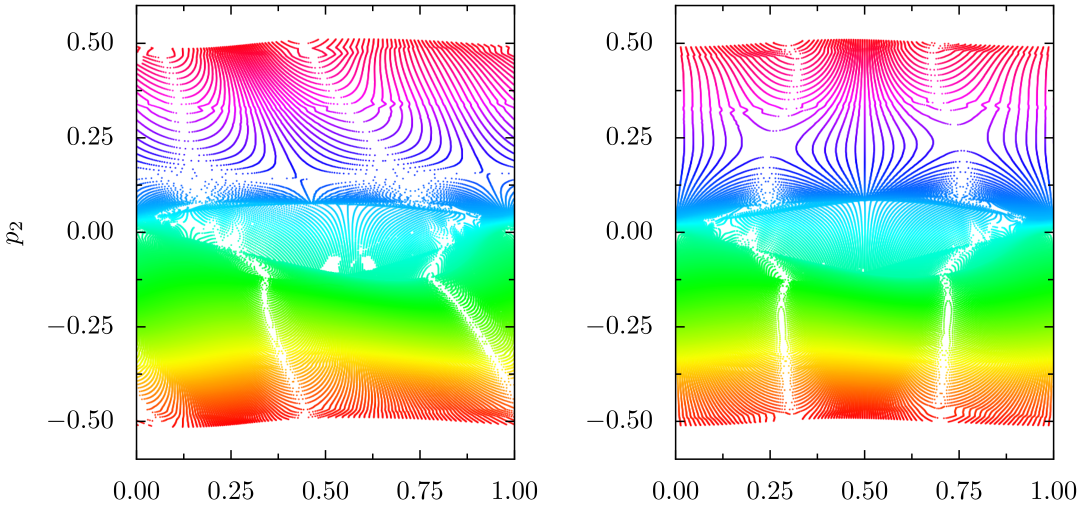

(c) $\xi = 0.15$

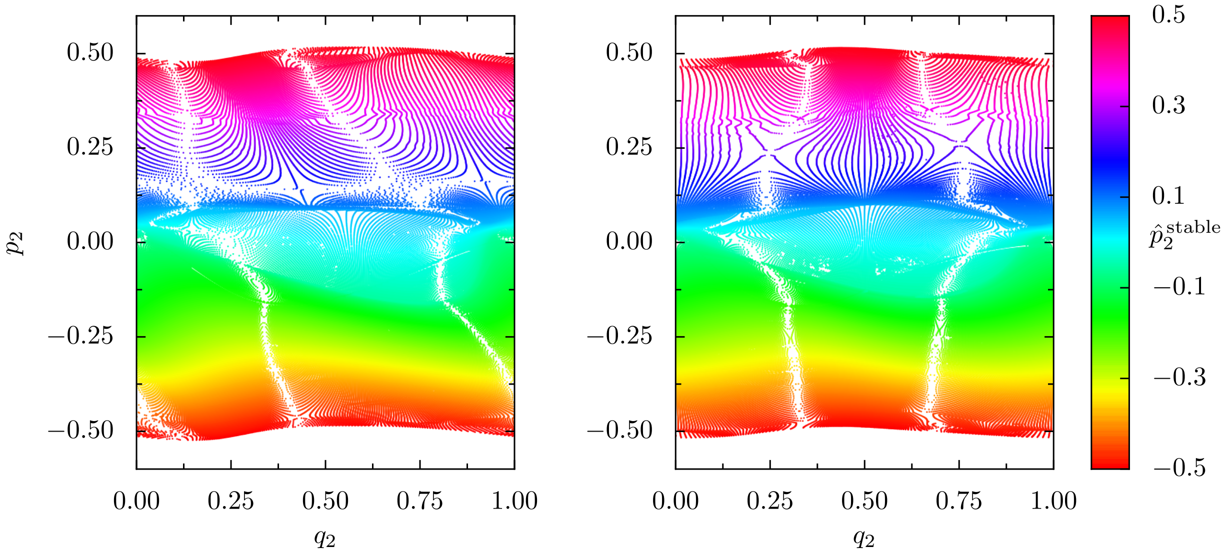

Figure 5.3: Projection to second degree of freedom of first (left column) and second (right column) upper intersection points. The colour encodes $\hat{p}_2$ of the involved stable manifold.

5.2.4 Cropping of manifolds

Based on the intersection points, the manifolds can be cropped like the example manifold in Fig. 4.4. To illustrate the process, the blue points describing this manifold are projected to the (p_1, q_2)-plane in Fig. 5.4(a). The first intersection points of this manifold are added as big yellow dots. These 4D intersection points are fitted with a polynomial of q_2 by `polyfit` from the NumPy package [80]. The order of the polynomial is the number of intersection points on this line, but at most 20. To guarantee reliable results we consider only manifolds with at least n_m intersection points and at least one point with $q_2 < q_{2,m}$ and one with $q_2 > 1 - q_{2,m}$. This prevents a wrong fit result close to $q_2 = 0, 1$. For $\xi \in \{0.1, 0.15\}$ the used values are $n_m = 9$, $q_{2,m} = 0.1$ and for $\xi = 0.01$ due to less deformations $n_m = 5$, $q_{2,m} = 0.2$. As visible in Fig. 5.3 these parameters exclude only a few manifolds for $\xi \in \{0.1, 0.15\}$ and for $\xi = 0.01$ mainly the region around $p_2 \approx 0.2$ with only homoclinic intersections. All manifolds that do not fulfil all of the above requirements are replaced by interpolated ones, cf. Sec. 5.2.2.

In addition to the determination of the extent of the manifold, this step interpolates equidistant points on the manifolds in q_1 and q_2, because it makes sense numerically and is useful for the following steps. The effect is shown in Fig. 5.4. While in (a) the points are highly non-uniform due to the growing process based on iterations, see Sec. 5.2.1, they are nicely distributed after the cropping process in (b). Note that the closer points for higher p_1-values are a side effect of the projection. In more detail, the cropping is done for each of 101 values for $q_2 \in [0, 1]$. For constant q_2 a line with 200 values in q_1 from the 1-torus to the intersection line is interpolated with `interp1d` from SciPy [79]. Hence, the cropping is done actually as each q_2-line ends at the intersection line, which is described by a polynomial as described above. The same procedure is done from the first to the second intersection line for the turnstile lobe. In both cases, the result of this one-parameter interpolation are points in the 4D phase space describing the relevant part of the manifold.

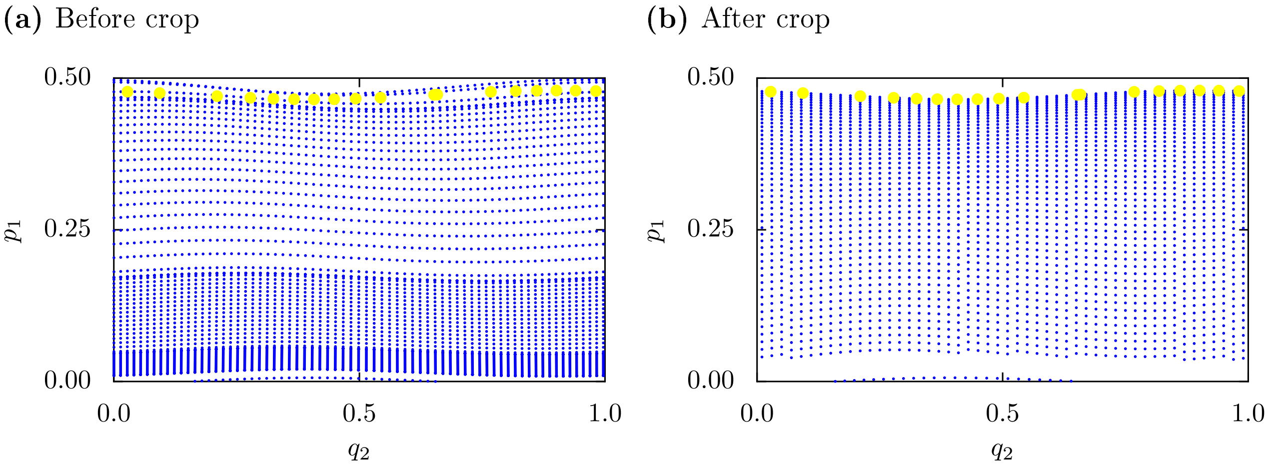

Figure 5.4: Projection to (p_1, q_2)-plane of upper unstable manifold with $\hat{p}_2 = 0.19$ at coupling $\xi = 0.1$ also shown in Fig. 4.4. The small blue dots are manifold points and the big yellow ones are the first intersection points with the family of stable manifolds. Note that for a clearer view in both figures not all computed points are plotted.

5.2.5 Intersections of a family of manifolds

This section describes the step from invariant manifolds parametrised by $\hat{p}_2$ to a section through this family at the parameter p_2^*. The physical motivation for this step and the definition of the section condition γ, Eq. (4.1), is given in Sec. 4.1. Note that a constant condition $p_2(q_2) = \gamma(q_2, p_2^*) = p_2^*$ is used in the following. For a different condition the distance to p_2^* would be replaced by the distance to $p_2(q_2, p_2^*)$.

At first, all cropped manifolds with $\hat{p}_2$ close to p_2^* are considered. The stronger the manifolds are deformed, i.e. the higher ξ, the broader the range in $\hat{p}_2$ of involved manifolds. For example, for $\xi = 0.1$ these are all manifolds with $\hat{p}_2\colon |\hat{p}_2 - p_2^*| < 0.08$. Secondly, just the points very close to p_2^* are kept. The maximal distance depends on the density of points in p_2, e.g. for $\xi = 0.1$ we choose all points with $p_2\colon |p_2 - p_2^*| < 0.003$. Note that, in order to get rid of interpolation problems at the periodic boundary condition in q_2, the points at $q_2 \gtrsim 0$ are duplicated with $q_2 + 1$ as new q_2-coordinate to $q_2 \gtrsim 1$. Similarly, points at $q_2 \lesssim 1$ are copied and shifted by -1.

Then, all these points are gathered according to their q_2-value. For each of the 101 values in $q_2 \in [0, 1]$ the corresponding points are interpolated linearly at $p_2 = p_2^*$. This is done with `griddata` from SciPy [79], which computes data on a regular grid from unstructured points in arbitrary dimensions. In our case, the parameters are the coordinates p_2, q_1 and q_2. The resulting 4D points all have exactly $p_2 = p_2^*$ and hence, can be treated as 3D points.

5.3 Volumes and points in 3D

This section explains different methods to compute a 3D volume enclosed by a 2D surface. The first approach in Sec. 5.3.1 reduces the problem to area computations in 2D planes. The second method in Sec. 5.3.2 and Sec. 5.3.3 makes use of uniformly distributed points that are classified as inside or outside of the volume.

5.3.1 Measure volumes

In the following, we examine the computation of a 3D volume enclosed by a 2D surface in a 3D space. The reduction from a 3D boundary in a 4D space is described in the previous section 5.2.5. The physical meaning and results for the used model system are given in Sec. 4.2.

We start with given boundary points in the space spanned by (p_1, q_1, q_2), like the black ones shown in Fig. 4.5, and assume a cylinder-like structure with periodic boundary conditions at least in q_2. Then, the volume computation can be reduced to area computations in slices of constant q_2. An example for such a slice is indicated by cyan points in Fig. 4.5, which are shown in the (p_1, q_1)-plane in Fig. 5.5. In (a) the area of the resonance zone is shown in grey and the turnstile lobe area in (b) in green. Both areas are in shape and value comparable to the 2D version shown in Fig. 2.1.

In order to use the computed boundary points as before, cf. Sec. 5.2.4, we use 101 of these q_2-slices with $q_2 \in [0, 1]$. The areas in the (p_1, q_1)-planes are bordered by 1D lines, which numerically define a polygon. Their area $A(q_2)$ is computed with Gauss's area formula [57] as explained in Sec. 2.1.

Finally, the volume is given by $V = \int_0^1 A(q_2)\,\mathrm{d}q_2$. The numerical computation of this integral is done by `trapz` from the NumPy package [80], which implements the trapezoidal rule.

The quality of the polygons can be improved by increasing the accuracy of the corners as they are the largest source of errors. To this end, an "upper" and a "lower" boundary is chosen. For turnstile lobes these are the bordering parts of the stable and unstable manifolds as indicated by red and blue lines in Fig. 5.5(b). The parts are fitted by a polynomial of order four, in case of the turnstile lobe, or linearly interpolated in case of the resonance zone. To improve the interpolation, especially close to $q_1 \approx 0, 1$, the points close to one are copied below zero and vice versa. Based on the fit or the interpolation, the left and right intersections are computed in the current 2D plane. Using these intersections leads to correct corners and hence, improves the result.

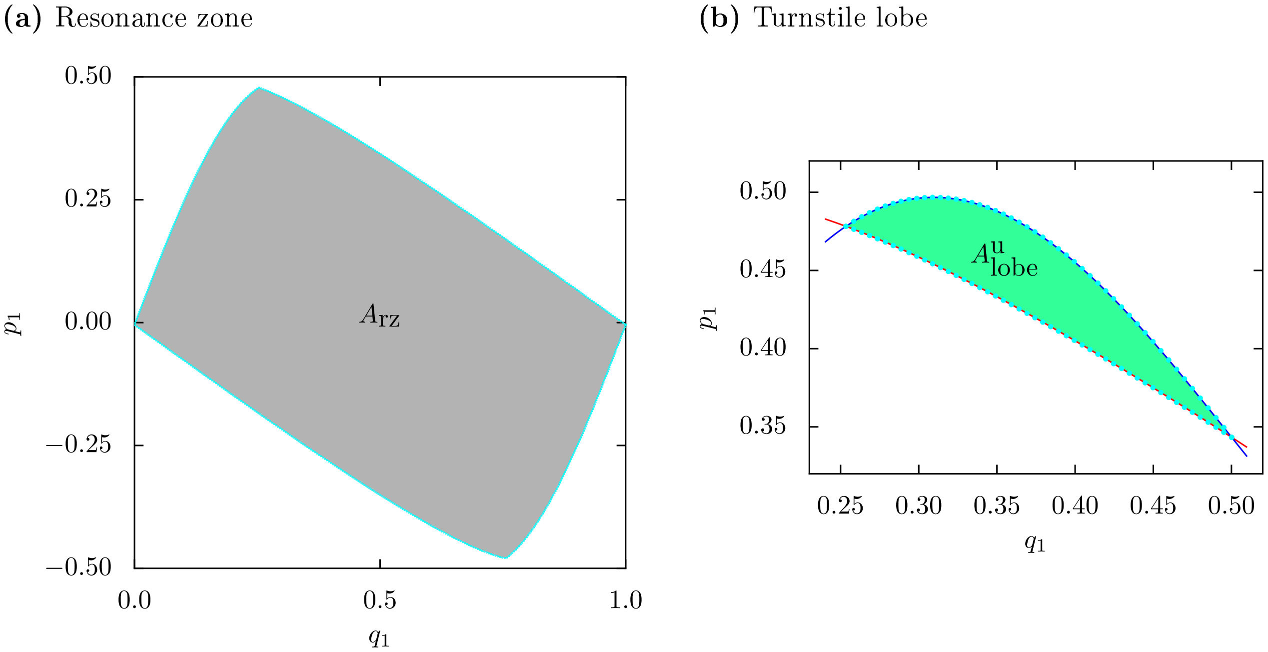

Figure 5.5: Cyan points from Fig. 4.5 in the (p_1, q_1)-plane. Part (a) shows the resonance zone and (b) the turnstile. The coloured regions mark the computed areas. In (b) additionally the fitting polynomials are shown as red and blue lines.

5.3.2 Find uniformly distributed points

One easy and convenient way to choose uniformly distributed points is to use a grid. Hence, we define a $(M_{p_1} \times M_{q_1} \times N_{q_2})$-grid of points on $[-0.5, 0.5) \times [0, 1) \times [0, 1)$. In order to utilize the slices in q_2 similar to Sec. 5.3.1, $N_{q_2} = 100$ is fixed. Given the sought overall number of points N_w, the number of points in p_1 and q_1 is $M_{p_1} = M_{q_1} = \sqrt{N_\mathrm{w}/N_{q_2}}$, which is rounded to the closest integer number. This results in $\tilde{N}_\mathrm{g} = M_{p_1} \cdot M_{q_1} \cdot N_{q_2}$ points.

Such a grid ensures the correct number of points for each value of q_2. As we are interested in points inside the boundary, for each q_2 needs to be checked which points of the grid are inside. As this is the same task as asking for any point to be in or out, the procedure is explained in the following section Sec. 5.3.3.

For large numbers of points $\tilde{N}_\mathrm{g}$ the process can be sped up by a rough precondition. This can be achieved by using the triangulation algorithm described in App. B. This algorithm has the ability to decide very fast whether a point is inside or outside, but always constructs a convex hull of the boundary points. Hence, the points inside the triangulation are good candidates to be really inside and none of the really inside points is rejected.

5.3.3 Decide in or out

In order to measure the transport, we need to decide whether a point is inside or outside the resonance zone before and after the iteration. This is done with the 3D barriers for each p_2^*-value as described in Sec. 4.3. While the points before the iteration are chosen with a p_2-value corresponding to the p_2^*-values of the borders, after the iteration a point can have any p_2-coordinate. Hence, for an iterated point the barrier section with the closest p_2^*-value is chosen.

The remaining three coordinates are then checked to be inside the corresponding 3D volume. For this, the problem is further reduced to the q_2-planes by choosing the closest plane. On the q_2-planes the point is tested to be inside the polygon spanned by the manifold points. This is done with the function `contains_points` of a Matplotlib path [81].

The accuracy of the method could be increased by interpolating the border instead of using the closest one. This applies on one hand for the section in p_2^* and on the other hand for the q_2-planes.

6 Summary and outlook

Phase space transport plays a crucial role in dynamical systems like chemical reactions [6] and plasma confinement [27]. Wile the transport within systems with only two degrees of freedom is well understood in terms of the turnstile mechanism, the generalization of this mechanism and its relevance in higher-dimensional systems is unclear. Since most systems have more than two degrees of freedom, our goal was to find a generalization of this mechanism to higher dimensions and demonstrate its relevance for transport. For this, we employ a 4D symplectic map as a generic higher-dimensional example system.

We present how the turnstile mechanism is relevant for the transport out of a resonance channel. While such channels are well understood in frequency space, they correspond to complicated structures in phase space. The skeleton of these structures consists of families of elliptic and hyperbolic 1-tori. Additionally, the interplay of such families and crossing resonances is discussed in terms of bifurcations [46].

In particular, we show that the invariant manifolds of a family of hyperbolic 1-tori act as the boundary of the corresponding resonance channel. We conclude that these are crucial structures for the transport. More precisely, we present their numerical computation and quantify the transport across this partial barrier: In order to construct such a barrier one has to compute (i) the family of 1-tori, (ii) their 2D invariant manifolds (iii) the intersections of manifolds and (iv) crop the manifolds at intersection lines. The resulting boundary encloses a 4D turnstile lobe, which in principle generalises the turnstiles of 2D systems to 4D. As the dynamics is very slow along the channel, it is reasonable to study the transport out of the channel locally, i.e. at different positions along the channel. This local transport is studied in 3D subspaces by sections of the boundary. Based on these local boundaries we approach the turnstile mechanism with two methods. On one hand, the volume of one turnstile lobe can be numerically calculated and serves as a prediction of the transport. On the other hand, the transport can be measured by starting many initial conditions inside the resonance zone and iterating them once. The results of both methods, termed volume and point method, respectively, are in very good agreement over a large range along the resonance channel. Hence, we conclude that the transport out of the channel is dominated by the turnstile mechanism in a regime far away from crossing resonances.

The same mechanism should apply for cantori, which have not been computed in generic higher-dimensional systems yet. For all kinds of barriers in higher dimensions, it is unknown which barrier has the smallest flux and thus, the strongest impact on the transport. Another subsequent question is the transport mechanism at crossing resonances. While there are studies in frequency space [82], the corresponding complex phase space structures need more investigation [83]. Furthermore, the construction of local partial barriers presented in this thesis could be used to study the transport along the channel. Although this topic is explored for over 50 years, there are still open questions [39,41,84]. If the complex transport phenomena in higher dimensions are better understood, this could lead to more precise predictions of chemical reaction speeds or improve the plasma confinement in a fusion reactor.

Appendix

A Ball method

In this appendix we present an alternative method to delimit a volume V in a n-dimensional space. The idea is based on a point cloud R as for example a chaotic orbit in a resonance layer. The union of n-spheres with radius r_{def} around all points is then considered the desired region. A sketch of the method is shown in Fig. A.1 with the volume V as grey region, the set R as blue points and the defining spheres with radius r_{def} as transparent blue areas.

The advantage of this method is that only very few assumptions are made. In particular, the exact boundary of the volume is not needed, but instead a set of points with sufficiently uniform density. In addition, it works in arbitrary dimensions and is easy to understand. In return, the results are not exact as there can arise gaps and overlapping spheres inside the volume and the spheres of points close to the boundary enlarge the volume necessarily. Furthermore, things get numerically cumbersome for high dimensions and/or many points in the set R.

For these reasons, the idea is not suited to determine the measure of the volume, but it can be useful to determine whether a test point x_T, shown in red in Fig. A.1, is in a given region or not. To this end, one could directly test whether the point x_T is inside one of the spheres. However, better results can be achieved by checking the number of defining points inside a larger sphere with radius ε around the test point, which is depicted as transparent red area. This prevents the loss of test points in small gaps between the defining spheres without rising the radius r_{def} too much, which would introduce large errors at the surface of the volume.

Such test points provide an opportunity to compute the measure of the volume. Similar as explained in Sec. 4.3, a volume can be determined by many uniformly distributed points, which are separated in inside and outside points.

In Sec. A.1 we discuss reasonable choices of the parameters as the radii of the involved spheres. Section A.2 presents some aspects of a numerical implementation.

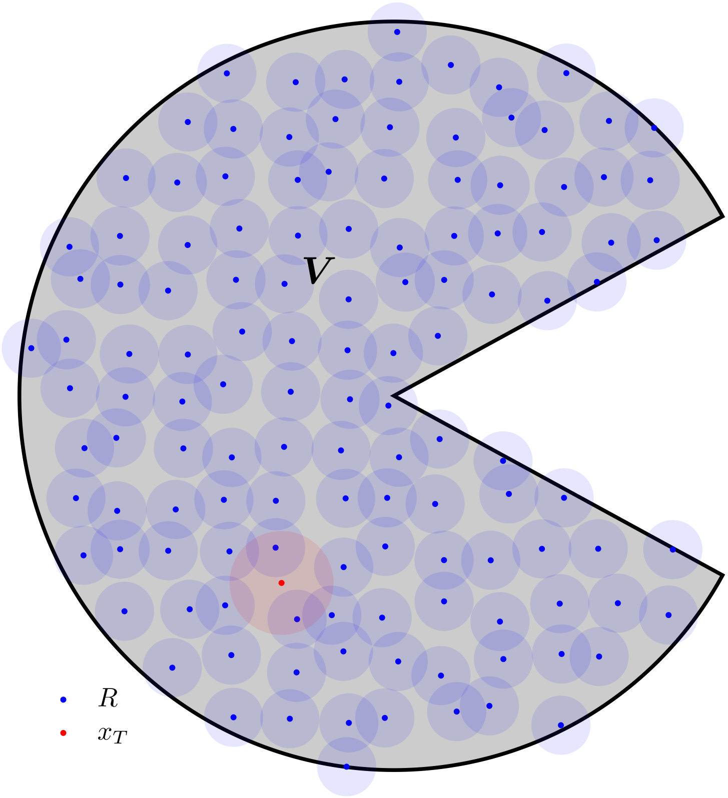

Figure A.1: Sketch of the ball method. The grey area is the volume V and the set R is depicted as blue points. The spheres of radius r_{def} around the defining points are shown as transparent blue circles. The test point x_T is shown in red surrounded by an enlarged transparent red circle.

A.1 Parameters

A reasonable choice for the radius r_{def} of the spheres is the mean distance between two points in the set R. This value can be determined numerically, which is a cumbersome task for many points. Fortunately, there are analytical results for the mean distance to the kth neighbour in a set of uniformly distributed points [85]

$$\langle r_k(N_u)\rangle = f(k,n) * (1/N_u)^{1/n} = \frac{\left[\Gamma(\frac{n}{2}+1)\right]^{1/n}}{\sqrt{\pi}} * \frac{\left[\Gamma(k+\frac{1}{n})\right]}{\Gamma(k)} * \left(\frac{1}{N_u}\right)^{1/n},$$

for a large number N_u of points per unit volume and the complete gamma function Γ. Hence, the mean distance between neighbouring points, $k=1$, in a set of N_R points in a volume V is

$$r_{\text{def}} = \langle r_1(N_R)\rangle = f(1,n) * \left(\frac{V}{N_R}\right)^{1/n} = \frac{\left[\Gamma(\frac{n}{2}+1)\right]^{1/n}}{\sqrt{\pi}} * \Gamma\left(1+\frac{1}{n}\right) * \left(\frac{V}{N_R}\right)^{1/d}.$$

Note that the inverse density $1/\varrho$ in the whole volume V/N_R is the same as in the unit volume $1/N_u$. Thus, one can use the quantity easier accessible in the respective application.

Now we define a test point x_T to be inside, if there are m points of the defining set R in a

n-dimensional ε-ball around it. The average number of defining points in this sphere is

$$\langle \tilde{n}(\varepsilon) \rangle = \varrho * B_\epsilon, \qquad \text{where} \quad B_\varepsilon = \frac{\pi^{n/2}}{\Gamma(\frac{n}{2}+1)} \varepsilon^n$$

is the volume of a d-dimensional sphere with radius ε. In order to consider also points x_T on the border to be inside, one could choose $m = \langle \tilde{n}(\varepsilon) \rangle / 2$. This reduces the problem to the choice of ε, which depends on the desired resolution of structures. At least, ε should be larger than the radius of the defining spheres $\varepsilon > r_{\mathrm{def}}$.

A.2 Numerics

A suitable structure for the computation of distances and neighbours is a tree. One implementation in Python is included in the spatial part of the SciPy package under the name `cKDTree`. This class provides functions to find all kth neighbours of a point and the corresponding distances (`query`) as well as to find all points in an ε-ball around a point (`query_ball_point`). The `query` function can also be used to compute the mean distance of the defining points.

B Triangulation method

Another method to describe a volume numerically based on a set R of discrete points is a triangulation. Introduced by Boris Delaunay in 1934 [86], a triangulation in the plane is done such that no point is inside the circumcircle of any triangle. Delaunay triangulations maximize the minimum angle of all the angles of the triangles [87]. An example is shown in Fig. B.1 where the desired volume is shown in grey, the points of the set R are the blue points and the edges of the triangles the blue lines.

This concept can be extended to arbitrary dimensions. The points are in general called vertices (singular: vertex) and the triangles are replaced by n-dimensional simplices (singular: simplex). Every n-simplex is spanned by $n + 1$ vertices. For instance, a simplex in 2D is a triangle and a 3-simplex is a tetrahedron. In the following, we focus on a 4D space and the corresponding 4-simplices, which are also called 5-cells as they are spanned by five vertices.

With a given triangulation it is numerically easy to compute the enclosed volume (Sec. B.1), start uniformly distributed points inside (Sec. B.2) and test efficiently whether a point is in or out (Sec. B.5). Furthermore, there are efficient algorithms available to find the triangulation of a set of points, see Sec. B.3.

While it does not matter whether the points are solely on the surface or distributed inside the volume, there is a strong limitation of the shape: a triangulation always describes the convex hull of the point set. This can be seen in Fig. B.1, where the cut-out is ignored and even the volume of the convex part is underestimated. The limitation to convex shapes can be overcome with the concept of α-hulls, see B.4, which is numerically more cumbersome. Another disadvantage of the triangulation method is the necessity of a full-dimensional volume as it does not work in subspaces, where the simplices collapse.

The last section B.6 deals with the visualisation of a 4-simplex in a 3D space in terms of sections.

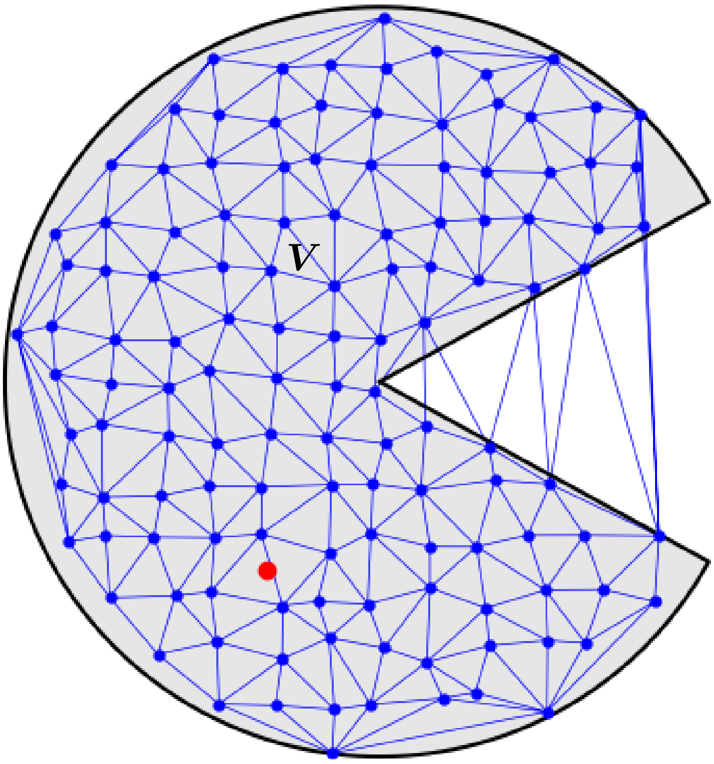

Figure B.1: Sketch of the triangulation method. The grey area is the volume V we aim to describe and the set R is depicted as blue points. The test point x_T is shown in red.

B.1 Compute the volume of a triangulation

The volume of a triangulation is simply the sum of all simplex volumes. The volume of a n-simplex is [88]

$$V_n = \left| \frac{1}{n!} \det(v_2 - v_1, v_3 - v_1, \dots, v_{n+1} - v_1) \right| \tag{B.1}$$

with the vertices v_i spanning the simplex.

B.2 Start uniformly distributed points inside a triangulation

In order to start uniformly distributed points inside a triangulation, one first properly picks a simplex and then finds a position in the simplex. To this end, the volume of each simplex is used to create a weighted random selection, which assures that larger simplices are picked more likely than smaller ones. Afterwards, inside the selected simplex a point is created randomly as follows [89, p. 568]. For every random point generate $d+1$ spacings S_i with $S_i \in [0, 1]$ and $\sum S_i = 1$. Then, every point $x = \sum S_i v_i$ with vertices v_i lies inside the simplex and the points

x will be uniformly distributed.

The advantage of this procedure is that every random point is inside the volume and hence, no additional check is needed. This can compensate for the higher computational effort, which arises particularly for high numbers of simplices.

B.3 Algorithm for Delaunay triangulation

In the plane, there are several algorithms to find the triangulation of a set of points [90]. In higher dimensions, one approach is to find the triangulation via the so-called "lifting" of the points by one dimension and to find the convex hull in this space [87]. In detail, each point x is given an extra coordinate equal to $|x|^2$, thus turning it into a hyper-paraboloid. After finding the convex hull of the paraboloid discarding the top cap, the points are mapped back to the lower dimensional space by deleting the last coordinate.

The convex hull can be found with the Quickhull algorithm [91–93]. An implementation in C for arbitrary dimensions is the qhull project, see `http://www.qhull.org`. For this project there are Python bindings available in the Delaunay class in the spatial subpackage of SciPy [79].

This class provides more than the computation of the triangulation. The function `find_simplex` finds the simplex that contains a given point. This can be used to determine whether a point like the red one in Fig. B.1 is inside the described volume or not. Details of the underlying method are given in Sec. B.5.

B.4 Non-convex volumes: α-hulls

A triangulation can approximate a non-convex shape by means of an α-hull, also called α-complex [94]. For this, a minimal sphere of radius r_{min} is put around each simplex. Then, simplices with $r_{\text{min}} > \alpha$ are removed. While the original idea and algorithm was developed for a plane, there followed a generalisation to 3D [95]. The concept can be generalized to higher dimensions by replacing the circles with n-balls.

The numerically difficult part is the computation of a minimal sphere around each simplex. As the problem of bounding spheres is of general interest, e.g. for computer graphics, there are several algorithms and implementations. Some of them are exact, but not very fast [96] while others compute very fast a nearly minimal sphere [97,98]. The methods in Refs. [96,97,99] are suited for applications in higher dimensions. A C++ implementation of the exact algorithm described in Refs. [99,100] can be found at Ref. [101] while a Python version is available as a github project [102].

B.5 Decide in or out: Barycentric coordinates

Barycentric coordinates help to decide whether a point is inside a simplex or not. More precisely, a point is inside, if its barycentric coordinates are positive and smaller than one [103, 104].
The conversion of Cartesian coordinates $\vec{x} = (x_1, x_2, \dots, x_n)$ to barycentric coordinates $\vec{\lambda} = (\lambda_1, \lambda_2, \dots, \lambda_{n+1})$ reads in terms of the Cartesian components of the simplex vertices $\vec{v}_1, \dots, \vec{v}_{n+1}$

$$\begin{aligned}\begin{pmatrix}\lambda_1\\ \vdots \\ \lambda_n\end{pmatrix} &= T^{-1}(\vec{x} - \vec{v}_{n+1})\\ \lambda_{n+1} &= 1 - \sum_{i=1}^{n} \lambda_i\end{aligned}$$

with

$$T = (\vec{v}_1 - \vec{v}_{n+1} \quad \dots \quad \vec{v}_n - \vec{v}_{n+1}).$$

Hence, the barycentric coordinates of the vertices are $\vec{v}_1 = (1, 0, \dots)$, $\vec{v}_2 = (0, 1, 0, \dots)$, etc.
In some applications it may be useful to determine the distance of a point to the triangulation or to one simplex. This can be done with the GJK-algorithm [105].

B.6 Visualize 4D simplices in a 3D slice

A 4-simplex is spanned by five vertices, which can be divided by a 3D slice in three different ways [106, Sec. I.IX.31]: On one side of the slice are three vertices and two on the other, 3 : 2 for short. The other two options are 4 : 1 and 2 : 2 with one point in the slice. The following table lists the originating objects in the slice.

case	points in slice	object
3 : 2	6	triangular prism
4 : 1	4	tetrahedron
2 : 2	5	square pyramid or tetrahedron

Bibliography

[1] H. Poincaré, “Sur le problème des trois corps et les équations de la dynamique”, Acta Math. **13**, 1–270 (1890).

[2] S. Gekle, J. Main, T. Bartsch, and T. Uzer, “Extracting multidimensional phase space topology from periodic orbits”, Phys. Rev. Lett. **97**, 104101 (2006).

[3] P. Schlagheck and A. Buchleitner, “Stable classical configurations in strongly driven helium”, Physica D **131**, 110–124 (1999).

[4] R. Paškauskas, C. Chandre, and T. Uzer, “Dynamical bottlenecks to intramolecular energy flow”, Phys. Rev. Lett. **100**, 083001 (2008).

[5] T. Uzer, C. Jaffé, J. Palacián, P. Yanguas, and S. Wiggins, “The geometry of reaction dynamics”, Nonlinearity **15**, 957–992 (2002).

[6] M. Toda, T. Komatsuzaki, T. Konishi, R. S. Berry, and S. A. Rice (editors) *Geometric Structures of Phase Space in Multidimensional Chaos: Applications to Chemical Reaction Dynamics in Complex Systems*, volume 130 of *Advances in Chemical Physics*, John Wiley & Sons, Inc., Hoboken, New Jersey (2005).

[7] A. Shojiguchi, C.-B. Li, T. Komatsuzaki, and M. Toda, “Fractional behavior in multidimensional Hamiltonian systems describing reactions”, Phys. Rev. E **76**, 056205 (2007), erratum ibid. **77**, 019902(E) (2008).

[8] H. Waalkens, R. Schubert, and S. Wiggins, “Wigner’s dynamical transition state theory in phase space: classical and quantum”, Nonlinearity **21**, R1–R118 (2008).

[9] R. S. MacKay and D. C. Strub, “Bifurcations of transition states: Morse bifurcations”, Nonlinearity **27**, 859–895 (2014).

[10] H. Waalkens and S. Wiggins, “Geometrical models of the phase space structures governing reaction dynamics”, Regul. Chaotic Dyn. **15**, 1–39 (2010).

[11] P. Pechukas and E. Pollak, “Classical transition state theory is exact if the transition state is unique”, J. Chem. Phys. **71**, 2062–2068 (1979).

[12] A. Bazzani, S. Siboni, and G. Turchetti, "Action diffusion for symplectic maps with a noisy linear frequency", J. Phys. A **30**, 27–36 (1997).

[13] M. N. Vrahatis, H. Isliker, and T. C. Bountis, "Structure and breakdown of invariant tori in a 4-D mapping model of accelerator dynamics", Int. J. Bifurcation Chaos **7**, 2707–2722 (1997).

[14] Y. Papaphilippou, "Detecting chaos in particle accelerators through the frequency map analysis method", Chaos **24**, 024412 (2014).

[15] E. J. N. Wilson, *An introduction to particle accelerators*, Oxford University Press, 1. publ. edition (2001).

[16] J. Boreux, T. Carletti, C. Skokos, and M. Vittot, "Hamiltonian control used to improve the beam stability in particle accelerator models", Commun. Nonlinear Sci. Numer. Simulat. **17**, 1725–1738 (2012).

[17] J. Laskar, "The chaotic motion of the solar system: A numerical estimate of the size of the chaotic zones", Icarus **88**, 266–291 (1990).

[18] R. I. Páez and C. Efthymiopoulos, "Trojan resonant dynamics, stability, and chaotic diffusion, for parameters relevant to exoplanetary systems", Celest. Mech. Dyn. Astron. **121**, 139–170 (2015).

[19] S. Udry and D. Pfenniger, "Stochasticity in elliptical galaxies", Astron. & Astrophys. **198**, 135–149 (1988).

[20] P. M. Cincotta, "Arnold diffusion: an overview through dynamical astronomy", New Astron. Rev. **46**, 13–39 (2002).

[21] C. Jung and E. E. Zotos, "Order and chaos in a three dimensional galaxy model", Mechanics Research Communications **69**, 45–53 (2015).

[22] W. S. Koon, M. W. Lo, J. E. Marsden, and S. D. Ross, "Heteroclinic connections between periodic orbits and resonance transitions in celestial mechanics", Chaos **10**, 427–469 (2000).

[23] N. Murray and M. Holman, "The role of chaotic resonances in the Solar System", Nature **410**, 773–779 (2001).

[24] J. Wisdom and M. Holman, "Symplectic maps for the N-body problem", Astron. J. **102**, 1528–1538 (1991).

[25] M. Dellnitz, O. Junge, W. S. Koon, F. Lekien, M. W. Lo, J. E. Marsden, K. Padberg, R. Preis, S. D. Ross, and B. Thiere, “Transport in dynamical astronomy and multibody problems”, Int. J. Bifurcation Chaos **15**, 699–727 (2005).

[26] A. H. Boozer, “Physics of magnetically confined plasmas”, Rev. Mod. Phys. **76**, 1071–1141 (2005).

[27] R. D. Hazeltine and J. D. Meiss, *Plasma Confinement*, Dover Publications New York, 2nd edition (2003).

[28] A. J. Lichtenberg and M. A. Lieberman, *Regular and Chaotic Dynamics*, Springer–Verlag, New York, second edition (1992).

[29] J. D. Meiss, “Thirty years of turnstiles and transport”, Chaos **25**, 097602 (2015).

[30] M. Dellnitz, G. Froyland, C. Horenkamp, and K. Padberg, “On the approximation of transport phenomena – a dynamical systems approach”, GAMM-Mitt. **32**, 47–60 (2009).

[31] R. Banisch, P. Koltai, and K. Padberg-Gehle, “Network measures of mixing”, Chaos **29**, 063125 (2019).

[32] R. S. MacKay, J. D. Meiss, and I. C. Percival, “Transport in Hamiltonian systems”, Physica D **13**, 55–81 (1984).

[33] S. Lange, A. Bäcker, and R. Ketzmerick, “What is the mechanism of power-law distributed Poincaré recurrences in higher-dimensional systems?”, EPL **116**, 30002 (2016).

[34] S. Lange, M. Richter, F. Onken, A. Bäcker, and R. Ketzmerick, “Global structure of regular tori in a generic 4D symplectic map”, Chaos **24**, 024409 (2014).

[35] L. H. Eliasson, “Perturbations of stable invariant tori for Hamiltonian systems”, Ann. Sc. Norm. Super. Pisa, Cl. Sci. **15**, 115–147 (1988).

[36] J. Pöschel, “On elliptic lower dimensional tori in Hamiltonian systems”, Math. Z. **202**, 559–608 (1989).

[37] À. Jorba and J. Villanueva, “On the normal behaviour of partially elliptic lower-dimensional tori of Hamiltonian systems”, Nonlinearity **10**, 783–822 (1997).

[38] À. Jorba and J. Villanueva, “The fine geometry of the Cantor families of invariant tori in Hamiltonian systems”, in C. Casacuberta, R. Miró-Roig, J. Verdera, and S. Xambó-Descamps (editors) “European Congress of Mathematics”, volume 202 of *Progress in Mathematics*, 557–564, Birkhäuser Basel (2001).

[39] V. I. Arnol'd, "Instability of dynamical systems with several degrees of freedom", Sov. Math. Dokl. **5**, 581–585 (1964).

[40] K. Kaneko and R. J. Bagley, "Arnold diffusion, ergodicity, and intermittency in coupled standard mapping", Phys. Lett. A **110**, 435–440 (1985).

[41] P. Lochak, "Arnold diffusion; A compendium of remarks and questions", in C. Simó (editor) "Hamiltonian Systems with Three or More Degrees of Freedom", volume 533 of *NATO ASI Series: C - Mathematical and Physical Sciences*, 168–183, Kluwer Academic Publishers, Dordrecht (1999).

[42] A. Malyshev and L. Chizhova, "Arnol'd diffusion in a system with 2.5 degrees of freedom: Classical and quantum mechanical approaches", J. Exp. Theor. Phys. **110**, 837–844 (2010).

[43] E. Todesco, "Analysis of resonant structures of four-dimensional symplectic mappings, using normal forms", Phys. Rev. E **50**, R4298–R4301 (1994).

[44] M. Gemmi and E. Todesco, "Stability and geometry of third-order resonances in four-dimensional symplectic mappings", Celest. Mech. Dyn. Astron. **67**, 181–204 (1997).

[45] H. Broer, H. Hanßmann, À. Jorba, J. Villanueva, and F. Wagener, "Normal-internal resonances in quasi-periodically forced oscillators: a conservative approach", Nonlinearity **16**, 1751–1791 (2003).

[46] F. Onken, S. Lange, R. Ketzmerick, and A. Bäcker, "Bifurcations of families of 1D-tori in 4D symplectic maps", Chaos **26**, 063124 (2016).

[47] E. Zehnder, "Generalized implicit function theorems with applications to some small divisor problems, II", Comm. Pure Appl. Math. **29**, 49–111 (1976).

[48] S. Wiggins, "On the geometry of transport in phase space I. Transport in k-degree-of-freedom Hamiltonian systems, $2 \leq k < \infty$", Physica D **44**, 471–501 (1990).

[49] M. Tabor, *Chaos and Integrability in Nonlinear Dynamics: An Introduction*, John Wiley & Sons, New York (1989).

[50] J. D. Meiss, "Symplectic maps, variational principles, and transport", Rev. Mod. Phys. **64**, 795–848 (1992).

[51] B. V. Chirikov, *Research concerning the theory of non-linear resonance and stochasticity*, CERN, Geneva (1971), translated at CERN from the Russian Preprint N 267, Institute of Nuclear Physics, Novosibirsk (1969).

[52] D. Bensimon and L. P. Kadanoff, “Extended chaos and disappearance of KAM trajectories”, Physica D **13**, 82–89 (1984).

[53] R. S. MacKay, “Equivariant universality classes”, Phys. Lett. A **106**, 99–100 (1984).

[54] R. S. MacKay, J. D. Meiss, and I. C. Percival, “Resonances in area-preserving maps”, Physica D **27**, 1–20 (1987).

[55] H. E. Lomelí and J. D. Meiss, “Resonance zones and lobe volumes for exact volume-preserving maps”, Nonlinearity **22**, 1761–1789 (2009).

[56] M. Firmbach and R. Ketzmerick, private communication (2020).

[57] W. H. Press, S. A. Teukolsky, W. T. Vetterling, and B. P. Flannery, *Numerical Recipes 3rd Edition: The Art of Scientific Computing*, Cambridge University Press, New York, NY, USA, 3 edition (2007).

[58] C. Froeschlé, “Numerical study of a four-dimensional mapping”, Astron. & Astrophys. **16**, 172–189 (1972).

[59] M. Richter, S. Lange, A. Bäcker, and R. Ketzmerick, “Visualization and comparison of classical structures and quantum states of four-dimensional maps”, Phys. Rev. E **89**, 022902 (2014).

[60] C. Froeschlé, “Numerical study of dynamical systems with three degrees of freedom. I. Graphical displays of four-dimensional sections”, Astron. & Astrophys. **4**, 115–128 (1970).

[61] P. A. Patsis and L. Zachilas, “Using color and rotation for visualizing four-dimensional Poincaré cross-sections: With applications to the orbital behavior of a three-dimensional Hamiltonian system”, Int. J. Bifurcation Chaos **4**, 1399–1424 (1994).

[62] R. Bartolini, A. Bazzani, M. Giovannozzi, W. Scandale, and E. Todesco, “Tune evaluation in simulations and experiments”, Part. Accel. **52**, 147–177 (1996).

[63] Y. P. Papaphilippou and J. Laskar, “Global dynamics of triaxial galactic models through frequency map analysis”, Astron. & Astrophys. **329**, 451–481 (1998).

[64] À. Jorba and M. Ollé, “Invariant curves near Hamiltonian-Hopf bifurcations of four-dimensional symplectic maps”, Nonlinearity **17**, 691–710 (2004).

[65] À. Jorba, “Numerical computation of the normal behaviour of invariant curves of n-dimensional maps”, Nonlinearity **14**, 943–976 (2001).

[66] J. Eldering, *Normally Hyperbolic Invariant Manifolds*, number 2 in Atlantis Series in Dynamical Systems, Atlantis Press, Paris (2013).

[67] N. Fenichel, "Persistence and smoothness of invariant manifolds for flows", Indiana Univ. Math. J. **21**, 193–226 (1972).

[68] M. W. Hirsch, C. C. Pugh, and M. Shub, *Invariant Manifolds*, number 583 in Lect. Notes Math., Springer Berlin Heidelberg (1977).

[69] M. Canadell Cano, *Computation of Normally Hyperbolic Invariant Manifolds*, Ph.D. thesis, Departament de Matemàtica aplicada i Anàlisi, Universitat de Barcelona (2014).

[70] M. Canadell and À. Haro, "Computation of quasiperiodic normally hyperbolic invariant tori: Rigorous results", J. Nonlinear Sci. **10.1007/s00332-017-9389-y** (2017).

[71] M. Canadell and À. Haro, "Computation of quasi-periodic normally hyperbolic invariant tori: Algorithms, numerical explorations and mechanisms of breakdown", J. Nonlinear Sci. **10.1007/s00332-017-9388-z** (2017).

[72] R. Bardakcioglu, A. Junginger, M. Feldmaier, J. Main, and R. Hernandez, "Binary contraction method for the construction of time-dependent dividing surfaces in driven chemical reactions", Phys. Rev. E **98**, 032204 (2018).

[73] B. V. Chirikov, "A universal instability of many-dimensional oscillator systems", Phys. Rep. **52**, 263–379 (1979).

[74] M. V. Berry, "Regular and irregular motion", volume 46 of *AIP Conference Proceedings*, American Institute of Physics (1978), reprinted in [107].

[75] F. Onken, *Bifurcations of families of 1-tori in 4D symplectic maps*, Masterthesis, Technische Universität Dresden, Fachrichtung Physik (2015).

[76] T. Schilling, *4D phase space and escape in van der Waals molecules*, Masterthesis, Technische Universität Dresden, Fachrichtung Physik (2017).

[77] R. Ketzmerick, private communication (2020).

[78] E. Castellá and À. Jorba, "On the vertical families of two-dimensional tori near the triangular points of the bicircular problem", Celest. Mech. Dyn. Astron. **76**, 35–54 (2000).

[79] P. Virtanen, R. Gommers, T. E. Oliphant, M. Haberland, T. Reddy, D. Cournapeau, E. Burovski, P. Peterson, W. Weckesser, J. Bright, S. J. van der Walt, M. Brett, J. Wilson, K. Jarrod Millman, N. Mayorov, A. R. J. Nelson, E. Jones, R. Kern, E. Larson, C. Carey, İ. Polat, Y. Feng, E. W. Moore, J. VanderPlas, D. Laxalde, J. Perktold, R. Cimrman, I. Henriksen, E. A. Quintero, C. R. Harris, A. M. Archibald, A. H. Ribeiro,

F. Pedregosa, P. van Mulbregt, and SciPy 1.0 Contributors, “SciPy 1.0: Fundamental Algorithms for Scientific Computing in Python”, Nature Methods (2020).

[80] T. E. Oliphant, *Guide to NumPy* (2006).

[81] J. D. Hunter, “Matplotlib: A 2d graphics environment”, Comput. Sci. Eng. **9**, 90–95 (2007).

[82] C. Efthymiopoulos and M. Harsoula, “The speed of Arnold diffusion”, Physica D **251**, 19–38 (2013).

[83] V. Gelfreich, C. Simó, and A. Vieiro, “Dynamics of symplectic maps near a double resonance”, Physica D **243**, 92–110 (2013).

[84] M. Guzzo and E. Lega, “The numerical detection of the Arnold web and its use for long-term diffusion studies in conservative and weakly dissipative systems”, Chaos **23**, 023124 (2013).

[85] P. Bhattacharyya and B. K. Chakrabarti, “The mean distance to the nth neighbour in a uniform distribution of random points: an application of probability theory”, Eur. J. Phys. **29**, 639–645 (2008).

[86] B. Delaunay, “Sur la sphère vide. A la mémoire de Georges Voronoï”, Bulletin de l’Académie des Sciences de l’URSS. Classe des sciences mathématiques et na 793–800 (1934).

[87] “Delaunay triangulation”, Wikipedia (2020), page Version ID: 951514115.

[88] “Simplex”, Wikipedia (2020), page Version ID: 957023821.

[89] L. Devroye, *Non-Uniform Random Variate Generation*, Springer-Verlag, New York (1986).

[90] D. T. Lee and B. J. Schachter, “Two algorithms for constructing a delaunay triangulation”, International Journal of Computer & Information Sciences **9**, 219–242 (1980).

[91] C. B. Barber, D. P. Dobkin, and H. Huhdanpaa, “The quickhull algorithm for convex hulls”, ACM Trans. Math. Softw. **22**, 469–483 (1996).

[92] R. Klein, *Algorithmische Geometrie: Grundlagen, Methoden, Anwendungen*, eXamen.press, Springer-Verlag, Berlin Heidelberg, 2 edition (2005).

[93] F. P. Preparata and M. Shamos, *Computational Geometry: An Introduction*, volume FIXNoVolumeFound of *Monographs in Computer Science*, Springer-Verlag, New York (1985).

[94] H. Edelsbrunner, D. Kirkpatrick, and R. Seidel, “On the shape of a set of points in the plane”, IEEE Transactions on Information Theory **29**, 551–559 (1983).

[95] H. Edelsbrunner and E. P. Mücke, “Three-dimensional alpha shapes”, ACM Transactions on Graphics **13**, 43–72 (1994).

[96] E. Welzl, “Smallest enclosing disks (balls and ellipsoids)”, in H. Maurer (editor) “New Results and New Trends in Computer Science”, Lecture Notes in Computer Science, 359–370, Springer, Berlin, Heidelberg (1991).

[97] J. Ritter, “An efficient bounding sphere”, 301–303 (1990), in [108].

[98] T. Larsson, “Fast and tight fitting bounding spheres”, in “SIGRAD 2008 on Interaction; November 27-28; 2008 Stockholm; Sweden”, Linköping Electronic Conference Proceedings, 27–30, Linköping University Electronic Press; Linköpings universitet (2008).

[99] K. Fischer, B. Gärtner, and M. Kutz, “Fast smallest-enclosing-ball computation in high dimensions”, in G. Di Battista and U. Zwick (editors) “Algorithms - ESA 2003”, Lecture Notes in Computer Science, 630–641, Springer, Berlin, Heidelberg (2003).

[100] B. Gärtner, “Fast and robust smallest enclosing balls”, in J. Nešetřil (editor) “Algorithms - ESA ’99”, Lecture Notes in Computer Science, 325–338, Springer, Berlin, Heidelberg (1999).

[101] B. Gärtner, “Miniball (C++)”, (2020), `https://people.inf.ethz.ch/gaertner/subdir/software/miniball.html`.

[102] K. Weddige, “Python implementation of Miniball”, (2020), `https://github.com/weddige/miniball`.

[103] E. Hille, *Analytic Function Theory*, volume 1, American Mathematical Soc. (1982).

[104] “Barycentric coordinate system”, Wikipedia (2020), page Version ID: 955941116.

[105] E. Gilbert, D. Johnson, and S. Keerthi, “A fast procedure for computing the distance between complex objects in three-dimensional space”, IEEE Journal on Robotics and Automation **4**, 193–203 (1988).

[106] Manning, Henry Parker, *Geometry Of Four Dimensions*, The Macmillan Company (1914).

[107] R. S. MacKay and J. D. Meiss, *Hamiltonian Dynamical Systems*, Adam Hilger, Bristol and Philadelphia (1987), (reprint selection).

[108] A. S. Glassner, *Graphics Gems*, Elsevier Science (1990).

Danksagung

Meine Promotion war eine sehr wichtige und spannende Phase meines Lebens. Dafür, dass es auch eine sehr schöne Zeit war, gebührt mein Dank sehr vielen Beteiligten. An erster Stelle danke ich meinem Doktorvater, Prof. Dr. Roland Ketzmerick, und zwar nicht nur für das interessante Thema und die wissenschaftliche Beratung, sondern auch für seine größtmögliche Unterstützung in allen Lebenslagen und sein Vertrauen. Ebenso danke ich Prof. Dr. Arnd Bäcker für die Bereitstellung vieler nützlicher Werkzeuge sowie für wissenschaftliche und hochschulpolitische Diskussionen. For further fruitful discussions I thank Jim Meiss, Henk Broer, Angel Jorba, Alex Haro and Alejandro Luque.

In meinen acht Jahren in der Arbeitsgruppe Computational Physics durfte ich mit vielen inspirierenden Menschen zusammenarbeiten. Einen großen Dank an Martin Richter, Steffen Lange, Steffen Löck, Normann Mertig, Matthias Michler, Clemens Löbner, Martin Körber, Martin Langer, Tom Schilling, Markus Firmbach, Felix Fritzsch, Konstantin Clauß, Jonas Stöber, Tabea Herrmann, Jan Schmidt und Gundula Schädlich. Insbesondere danke ich Felix Fritzsch, Markus Firmbach, Konstantin Clauß und Steffen Lange für das Korrekturlesen dieser Arbeit.

Persönlich danke ich meiner Schwester Roxana Onken, die mich oft entlastet hat. Ebenso Anna Lasch, die stets zur Stelle ist, wenn es mal brennt. Zu guter Letzt bin ich meinem Ehemann Sebastian dankbar. Dafür, dass er sich so geduldig und liebevoll um unsere zwei wunderbaren Töchter kümmert, dass er immer um Gerechtigkeit bemüht ist und dafür, dass er mich auch gestresst und übermüdet erträgt. Danke für alles.

Hardware and software used for this thesis:

- Taurus at the ZIH of the TU Dresden
- Python (3.6) packages:
  - Numpy (1.14.3)
  - Scipy (1.1)
  - Cython (0.28.3)
  - mayavi (4.6.2)
  - PyX (0.14.1) and PyXgraph
- MongoDB (4.0.18) and PyMongo (3.7)

Erklärung

Hiermit versichere ich, dass ich die vorliegende Arbeit ohne unzulässige Hilfe Dritter und ohne Benutzung anderer als der angegebenen Hilfsmittel angefertigt habe; die aus fremden Quellen direkt oder indirekt übernommenen Gedanken sind als solche kenntlich gemacht. Die Arbeit wurde bisher weder im Inland noch im Ausland in gleicher oder ähnlicher Form einer anderen Prüfungsbehörde vorgelegt.
Die vorliegende Dissertation wurde unter der Betreuung von Prof. Dr. Roland Ketzmerick am Institut für Theoretische Physik der Technischen Universität Dresden angefertigt. Es haben keine früheren erfolglosen Promotionsverfahren stattgefunden. Ich erkenne die Promotionsordnung des Bereiches Mathematik und Naturwissenschaften an der Technischen Universität Dresden vom 23. Februar 2011 mitsamt der Änderungen vom 15. Juni 2011, vom 18. Juni 2014, sowie vom 23. Mai 2018 an.

Franziska Hübner
Dresden, Juni 2020